Table of Contents

List of Figures

Chapter 1

Glossary

EL Entrainment Layer

ML Mixed Layer

CBL Convective Boundary Layer

LES Large Eddy Simulation

FFT Fast Fourrier Transform

Ri Richardson Number , the bulk Richardson Number is $\frac{gh}{\overline{\theta}_{ML}} \frac{\Delta\theta}{w^{*2}}$, $\Delta\theta = \overline{\theta}(h_1) - \overline{\theta}(h_0)$

Chapter 2

Introduction

2.1 Motivation

Atmospheric boundary layer growth by entrainment driven by convecive thermals acting against a stable lapse rate or inversion makes for an interesting topic. (list of studies) It is a subsection of a broader topic of interest in geophysical fluid dynamics ie that of entrainment of a fluid into a turbulent fluid accross a density interface. It involves the buoyant suppression of buoancy driven plumes, and subsequent trapping and mixing of the more buoyant air from accross the buoyancy/density gradient or jump.

Boundary layer height and prediction there of are important for calculating tracer IE pollutant concentrations and the limiting sizes of turbulant structures. (Steyn Baldi Hoff) Also the rate at which the boundary layer entrains air from above enables calculation of the rate at which tracers transported long range are drawn in an mixed with the air we breathe.

In combination with the lifting condensation level, knowledge of entrainment layer depth allows predictions pertaining to the formation of cumulous clouds for example if the EL is above the lifting condensation a high percentage of cloud cover would be expected. Parametrizations for both CBL growth and EL depth are used in Mesoscale models and GCMs. Further along the vein of prediction and parametrization it is an attractive goal to develop a robust set of scales such that a similarity theory as analogous to MO theory for the surface for this region could be developed (quote from GarciaMellado, Sorbjan1999).

Bulk analyitical models underly certain parametrizations and scaling relatiohships (Traumner) and are validated by measurements and output from LES and DNS models. The two important categories referenced here are the zero order whcih assume an infinitessimly thin entrainment layer and the 1st order which includes an entrainment layer of finite depth and there is discussion in the literature as to whether explicit consideration of the EL depth is required. Both types typically relies on the simplified reynolds averaged thermodynamic equation

$$\frac{D\overline{\theta}}{Dt} = -\frac{\partial \overline{w'\theta'}}{\partial z} \tag{2.1}$$

relating average potential temperature to average vertical turbulent potential temperature flux, as well as idealized vertical profiles for both. So verification of the resulting entrainment equation by LES using ensemble averaged θ and $w^{'}\theta^{'}$ logically follows. So far, horizontal and time averaging has been used but we will run an ensemble of cases, and apply true ensemble averaging as well as horizontaly averaging to get smooth vertical profiles.

Studies in which the scaling relation or parametrizations for Δh is verified (Deardorf tank, SullMoengStev, Fed, BrooksFow, GarciaMellado) refer to the potential temperature or buoyancy inversion region but do not define the entrainment layer EL limits it in terms of the vertical average potential temperature profile. So it seemed like an obvious opportunity to try.

Convective boundary layer entrainment depends most critically on surface heat flux and upper lapse rate (Fed04 from Sorbjan1996) but so far similar studies (ie those verifying the entrainment rate and entrainment layer depth relations) have focused on acheiving a range of Richardson numbers by varying $\overline{w'\theta'}_s$ and the temperature jump (SullMoeng, BrooksFow), whereas Fedorovich varied the upper lapse rate while maintaining a constant surface heat flux. We choose to vary these two key external parameters, allowing a $\Delta\theta$ to develop with penetrative convection and entrainment. Garcia and mellado came out after our runs were done, but they seem to vary both.

Sullivan and Pattons resolution study showed the sensitivity of the heat flux and potential temperature profiles to grid size in particular in the vertical and in the entrainment layer. This strongliy influenced our decision to apply a higher resolution within the entrainment layer than the previous similar LES studies.

2.2 Relevant Background

2.2.1 The Convective Boundary Layer (CBL)

The convective boundary layer over land starts to grow at rapidly at sunrise reaching a peak at midday with the peak in solar irradiation. Convective turbulence and the dominant upward vertical motions die down towards the evening and as surface cools. In the morning as the surface warms relative to the environment instability causes thermals to develop and rise with buoyancy driven momentum. The are adjacent to and closely associated with cooler slower downdraughts. The thermals or thermal plumes are of uniform potential temperature and tracer concentration at their cores and entrain surrounding air laterally as they rise, as well as trapping and mixing in stable warm from above. (Stull [17], **?** [**?**]) In cases of stromg convection, Buoyantly driven turbulence dominates and shear is insignificant. (**?** [**?**]) Thermals rise, overshoot their natural buouancy level and overturn or recoil, trapping pockets (or whisps) of warm stable air which then becomes turbulently mixed. This overshoot and subsequent entrainment of the warmer air from aloft augments the warming cased by the surface heat flux. A potential temperature jump results, but an inversion may also be

imposed and strengthened for example by subsidence.
Lidar images show the overall structure of the convective boundary layer (CBL) with the rising thermals, impinging on the air above. (**?** [**?**], Traumner et al. [20]) This has been effectively modelled by large eddy simulation by Schmidt and Schumann in [12] where using horizontal slices at various levels show how the thermals apparently merge with some distance from the surface. At the top of the CBL they observed thermal tips impinging with concurrent periferal downward motions. This is supported in the visual tools used by Sullivan et al. [19]. They show vertical cross sections of relatively cooler thermal plumes and trapped warmer air as well as the closely associated upward motion of cooler air and downward motion of warmer air.

On average these convective turbulent structures create a mixed layer ML with eddy scales cascading from approximately the CBL height to molecular diffusion according to the Kolmagorav power law. Here potential temperature is close to uniform and average heat flux is positive and decreasing. Warming is from both the surface heat flux ($w^{'}\theta^{'}_{s}$) and the flux of entrained stable air at the inversion ($w^{'}\theta^{'}_{i}$). Since the Mixed Layer (ML) is mainly comprised of warm updraughts and cool downdraughts the $w^{'}\theta^{'}_{s}$ is on average positive, turning negative in the entrainment layer EL where the updraughts are now relatively cool and there is downward movement of warm air from above. Above the ML the air becomes more stable with altitude and on average this reflects as transition from a uniform ML potential temperature to the stable lapse rate. A peak in the gradient represents regions where thermal plumes are at points higher than their natural buoyancy level.

Nelson et al. in [11] outlines the stages of CBL growth as the sublayers of the nocturnal boundary layer are entrained, untill the previous days capping inversion is reached and a quasi-steady state growth is attained. The EL depth relative to CBL height varies throughout these stages and its relationship to scaled entrainment rate forms a hysteresis. The studies based on LES output typically represent this last quasi-steady phase, since there is usually a constant heat flux working against an inversion and or a stable lapse rate. (Schmidt and Schumann [12], Sorbjan [13], Sullivan et al. [19], Federovich et al. [6], Brooks and Fowler [3])

2.2.2 Convective Boundary Layer Height

The ML is fully turbulent with an on average uniform temperature. Aerosol and water vapour concentrations decrease dramatically with transition to the stable upper atmpsphere. So any of these characterstics can support a definition of CBL height. Nelson et al. define height in terms of percentage of ML air and identified by eye from Lidar backscatter images in [11]. Traumner et al. used the four most commonly used automated methods applied to Lidar images: identifying a suitable threshold value above which the air is categorized as ML air, locating the point of minimum (largest negative) vertical gradient, fitting an idealized curve to the profile from which a location of minimum vertical gradient can be easily determined, and using wavelet covariance in [20].

The use of Lidar dominates studies based on measurement. In numerical modelling studies there is the advantage of having plently of points to average over as well as the ability to directly measure veritcal heat flux. Brooks and Fowler [3] applied their wavelet technique to local vertical tracer profiles in their LES study as well as using the gradient method (IE locating the point of minimum vertical gradient). For comparison they also used the point of miniumum average vertical heat flux ($\overline{w'\theta'}$). This last definition has been the common in LES studies and has frequently been referred to as z_i (inversion height) (Deardorff et al. [5], Sorbjan [14], Federovich et al. [6]). Sullivan et al. [19] clarified that this point did not correspond to the average point of maximum vertical potential temperature gradient, whereas the upper extrema of the four vertical heat flux quadrants (upward moving warm air, dowward moving warm air, upward moving cool air, downward moving cool air) more or less did. They defined CBL height based on local vertical potential temperature gradients and applied horizontal averaging as well as other methods, including two based on the average vertical heat flux ,for comparison.

None of the LES studies so far define the height in terms of the average potential temperature profile even though bulk models, from which CBL growth parametrizations stem, rely on an idealized version thereof. Garcia and Mellado do include it as one of their measures of CBL height in their direct numerical simulation study (**DNS!**) [7].

2.2.3 Convective Boundary Layer Growth by Entrainment

In the quasi-steady regime the CBL grows by trapping pockets of warm stable air between or adjacent to impinging thermal plumes. Traumner et al. [20] summarize two relevant buoyancy driven regimes of entrainment:

Non turbulent fluid can be engulfed between or in the overturning of thermal plumes. This kind of event was seen by Sullivan et al. in [19] when the iversion was weak. Traumner et al.'s observations in [20] support this.

Impinging thermal plumes distort the inversion interface dragging whisps of warm stable air down at their edges or during recoil under a strong inversion or lapse rate. This type of event is supported by the finding of both Sullivan et al. [19] and Traumner et al. [20].

Under atmospheric conditions shear induced stabilities do occur, and in some laboratory studies under very high stability the breaking of internal waves have been observed. Both processes are believed to result in some entrainment but we dismiss them since the former is insignificant and the latter has not so far been observed in measurements or modeled output of the atmospheric CBL (Traumner et al. [20], Sullivan et al. [19])

2.2.4 The Convective Boundary Layer Entrainment Layer

The ML is fully turbulent but at the top is characterised by stable air with intermittant turbulence due to the higher reaching thermal plumes. Garcia and Mellado demonstrate that the entrainment layer EL is subdivided in terms of length and buoancy scales. That is to say, the lower region is comprised of mostly turbulent air with pockets of stable warmer air that are quickly mixed, and so scales with the convective scales. Whereas the upper region is mostly stable apart from the impinging thermal plumes so scaling here is more influenced by the lapse rate γ.

In the EL the average vertical heat flux ($\overline{w'\theta'}$) switches sign relative to in the ML. The fast updraughts are now cool (quadrant II) relative to the average potential temperature and there is downward movement of warm air (quadrant IV) from the stable layer above. In their analysis of the four flux quadrants **SullMoengStev!** concluded that overall dynamic in this region is downward motion of warm air since the other three quadrants effectively cancel.

In terms of tracer concentration and for example based on a Lidar backscatter profile, there are two ways to conceptually define the entrainment layer (EL). It can be thought of as the range in space (or time) over which local height varies. (**?** [**?**]) There is also a local region over which the concentration (or back scatter intensity) transitions from ML to upper free atmospheric value (Traumner et al. [20]). The latter can be estimated using both curve-fitting and wavelet techniques.(Traumner et al. [20], Steyn et al. [15], Brooks and Fowler [3]). Traumner et al. [20] compared the two, found them to differ and seem to favour the latter based on how correlated the corresponding scaling relations were.

Brooks and Fowler apply a wavelet technique to tracer profiles for the determination of EL limits, in their LES study in [3]. But it is more common in numerical modelling and laboratory studies for the EL limits to be defined based on the average vertical heat flux ($\overline{w'\theta'}$) IE the points at which it goes from positive to negative and the point at which it goes from negative to zero. (Deardorff et al. [5] ,Federovich et al. [6], Garcia and Mellado [7]). Bulk first order models assume the region of negative $\overline{w'\theta'}$ coincides with the region where the average potential temperature $\overline{\theta}$ transitions from the ML value to that corresponding to the stable lapse rate above γ. (Deardorff [4], [6] [6]). But no modelling studies use the vertical $\overline{\theta}$ to define the entrainment layer (EL). Since the ML $\overline{\theta}$ from a numerical model is not strictly constant (Federovich et al. [6]), for the lower EL limit, a threshold value for $\overline{\theta}$ or its vertical gradient would have to be chosen. Brooks and Fowler encountered inconsistencies when determining the EL limits from the average tracer profile [3]. But the their tracer profile is different to a simulated $\overline{\theta}$ profile whose ML value increases in time predictably based on the vertical heat flux from the surface and the CBL top or inversion.

2.3 Modelling the Convective Boundary Layer and Entrainment Layer

2.3.1 Bulk Analytical Models

Bulk analytical models for the Convective Boundary layer (CBL) can be subdivided into: (i) zero order and (ii) first order bulk models.

Zero order bulk models assume a Mixed Layer (ML) of uniform potential temperature ($\overline{\theta}_{ML}$) topped by an infinitessimally thin layer accross with there is a temperature jump ($\Delta\theta$). A constant lapse rate above the inversion is assumed. The assumed vertical heat flux ($\overline{w,\theta,}$) profiles are linearly decreasing from the surface up, reaching a maximum negative $\overline{w,\theta,}_i$ value proportional to the surface value (usually -.2) at the temperature inversion and going to zero accross the jump. Evolution equations for the evolution of CBL height, $\overline{\theta}_{ML}$ and $\Delta\theta$ are deriven this basis.
For example, if the CBL height is rising as a result air is being drawn in from the stable layer above and decreasing in enthalpy. The decrease in enthalpy

is so $c_p \rho \Delta\theta \frac{dh}{dt}$ per unit of horizontal area. Since above the inversion is stable **?** in [**?**] equates this enthalpy loss to the average vertical flux at the inversion IE

$$\Delta\theta \frac{dh}{dt} = -\overline{w'\theta'}_i \tag{2.2}$$

The warming rate of the ML is arrived at using the simplified reynolds averaged conservation of enthalpy

$$\frac{\partial \overline{\theta}_{ML}}{\partial t} = -\frac{\partial}{\partial z} \overline{w'\theta'} \tag{2.3}$$

which based on the assumed constant slope of the vertical heat flux becomes

$$\frac{\partial \overline{\theta}_{ML}}{\partial t} = \overline{w'\theta'}_i - \overline{w'\theta'}_0 \tag{2.4}$$

and the evolution of the temperature jump ($\Delta\theta$) depends on the rate of CBL height (h) increase, the upper lapse rate γ and the warming rate of the ML

$$\frac{d\Delta\theta}{dt} = \gamma \frac{dh}{dt} - \frac{d\overline{\theta}_{ML}}{dt} \tag{2.5}$$

An assumption about the vertical heat flux at the inversion, such as the entrainment ratio, closes this set.

$$\frac{\overline{w'\theta'}_i}{\overline{w'\theta'}_0} = -.2 \tag{2.6}$$

? [**?**]

The relevant quantities are idealized ensemble averages. There is some variation among such models for example the rate equation for h (entrainment relation) can be derived based on the turbulent kinetic energy budget (Federovich et al. [6]). But they are all based on the simplified $\overline{\theta}$ and $\overline{w'\theta'}$ profiles outlined above.

First order models assume an Entrainment layer (EL) of finite depth at the top of the ML, defined by two heights: the top of the ML (h_0) and the point where free atmospheric characteristics are resumed (h_1). The derivations are more complex and examples of simplifying assumptions about the EL are: $\Delta h = h_1 - h_0 = Constant$, Δh or maximum overshoot distance $d \propto \frac{w^*}{N}$ where w^* is the relevant vertical velocity scale and $N = \sqrt{\frac{g}{\overline{\theta}}\frac{\partial\overline{\theta}}{\partial z}}$ is the Brunt-Vaisalla frequency and that between h_0 and h_1 $\overline{\theta} = \overline{\theta}_{ML} + f(x,t)\Delta\overline{\theta}$ where $f(x,t)\Delta\overline{\theta}$ is a dimensionless shape factor (Deardorff [4], Stull [16]).

Although development of these models is beyond the scope of this thesis, mention of them is necessary to give context to the scaling parameters and relationships under consideration.

2.3.2 Numerical Simulations

(Here!)
Direct Numerical Simulataions (**DNS!**) solve the Navier Stokes Equations without use of sub grid scale closure, i.e. all range of spatial and temportal turbulence must be resolved from the A Large Eddy Simulation (LES) filters out the smaller scales leaving them to a sub grid scale closure model. General Circulation Models (**GCM!**) can model global processes, so their subgrid scale can span the an LES domain, and they use a grid based on spherical coordinates.

(paper from Douws 571c justifying LES use)
LES has steadily, repeatedly been used to better understand the CBL since **?** applied this relatively new method in [**?**] for this purpose. Sullivan et al. in [19], Federovich et al. in [6] and Brooks and Fowler in citeBrooksFowler2 used it to observe the structure and scaling behaviour of the EL.

The technique has been widely used to closely simulate measurement campaigns as well as more idealized conditions whereby scaling relations, parametrizations and analystical models can be tested. (references? tie in to what i'm using it for)

cover initial conditions here, ie delta theta vs constant lapse rate

2.4 Scales of the CBL and Entrainment Layer

2.4.1 Length Scale

2.4.2 Convective Velocity Scale

Given an average surface heat flux ($\overline{w\text{'}\theta\text{'}_s}$) a surface buoyancy flux can be defined as $\frac{g}{\overline{\theta}}\overline{w\text{'}\theta\text{'}}$ from which the convective velocity scale is obtained by multiplying by the appropriate length scale. Since the result is in $\frac{m^3}{s^3}$ a cube root is applied.

$$w^* = \left(\frac{gh}{\overline{\theta}}\overline{w\text{'}\theta\text{'}}\right) \tag{2.7}$$

? ([**?**]) confirmed that this effectively scaled the vertical turbulent velocity perturbations in the CBL.

this scales the vertical velocity perturbations in the cbl. can i tie in something about the joint distributions of theta and w? ie talk about the $\theta^{'}$ and $w^{'}$ for example $w^{'}$ are driven by $\overline{w'\theta'}$ must refer to Sorbjan

2.4.3 Convective Time Scale

It logically follows that the time for a plume to reach the top of the CBL is

$$\tau = \frac{h}{\left(\frac{gh}{\overline{\theta}}\overline{w\text{'}\theta\text{'}}\right)} \tag{2.8}$$

where h is CBL height.
mention the brunt vaisalla time scale as used by Fed and Garcia

2.4.4 Convective Temperature Scale

here I must refer to sorbjan. $\theta^{'}$ is influenced by $\overline{w'\theta'}_s$ in the lower part of the CBL but by γ in the upper CBL and EL

2.4.5 Richardson Number

The Flux Richardson (R_f) expresses the balance between turbulent mechanical energy and buoyancy. It's obtained from the ration of these two terms in the Turbulent Kinetic Energy budget equation ([17]):

$$\frac{\partial \overline{e}}{\partial t} + \overline{U}_j \frac{\partial \overline{e}}{\partial x_j} = \delta_{i3} \frac{g}{\overline{\theta}} \left(\overline{u_i^{,} \theta^{,}} \right) - \overline{u_i^{,} u_j^{,}} \frac{\partial \overline{U}_i}{\partial x_j} - \frac{\partial \left(\overline{u_j^{,} e^{,}} \right)}{\partial x_j} - \frac{1}{\overline{\rho}} \frac{\partial \left(\overline{u_i^{,} p^{,}} \right)}{\partial x_i} - \epsilon \tag{2.9}$$

$$R_f = \frac{\frac{g}{\overline{\theta}} \left(\overline{w^{,} \theta^{,}} \right)}{\overline{u_i^{,} u_j^{,}} \frac{\partial \overline{U}_i}{\partial x_j}} \tag{2.10}$$

Assuming horizontal homogenaiety and neglecting subsidence

$$R_f = \frac{\frac{g}{\overline{\theta}} \left(\overline{w^{,} \theta^{,}} \right)}{\overline{u^{,} w^{,}} \frac{\partial \overline{U}}{\partial z} + \overline{v^{,} w^{,}} \frac{\partial \overline{V}}{\partial z}} \tag{2.11}$$

Applying first order closer to the flux terms (i.e. assuming they are proportional to the vertical gradients) gives the gradient Richardson Number (R_g)

$$R_g = \frac{\frac{g}{\overline{\theta}} \frac{\partial \overline{\theta}}{\partial z}}{\left(\frac{\partial \overline{U}}{\partial z} \right)^2 + \left(\frac{\partial \overline{V}}{\partial z} \right)^2} \tag{2.12}$$

which is usually used to express the balance between shear and buoyancy driven turbulence, but in the EL buoancy acts to supress turbulence. Applying a bulk approximation the to the numerator, and expressing it in terms of scales yields a ratio of two square of time scales

$$R_g = \frac{\frac{g}{\overline{\theta}} \frac{\partial \overline{\theta}}{\partial z}}{\frac{U^{*2}}{L^2}} = N^2 \frac{L^2}{U^*} \tag{2.13}$$

and applying the bulk approximation to both the numerator and the denomnitor yields

$$R_b = \frac{\frac{g}{\overline{\theta}}\Delta\overline{\theta}L}{U^*} \tag{2.14}$$

A natural choice of length and veloctiy scales for the CBL are h and w^*. **?** ([**?**]) suggested and confirmed a relationship between the entrainment rate and this form of Richardson number based on tank experiments. This parameter can be justified and arrived at by considering the principal forcings of the system, or from non-dimensionalizing the entrainment relation deriived analyitically, i.e. ([**?**])

$$w_e \propto \frac{\overline{w'\theta'}_s}{\Delta\overline{\theta}} \tag{2.15}$$

$$\frac{w_e}{w^*} \propto \frac{\overline{w'\theta'}_s}{\Delta\overline{\theta}w**} = Ri_b^{-1} \tag{2.16}$$

In one or other of its forms this parameter has become central to any study on CBL entrainment ([19], [6], [20], [3])

2.4.6 Relationship of Entrainment Rate and Entrainment Layer Depth to Richardson Number

equilibrium entrainment regime

derivation of the scaled entrainment relation to Ri by integration of the thermodynamic equation over an infinitessimely small layer.

mention of two main power law relationships

sequence of publications katophilips, deardorff, sullmoeng, fed, bandf

two ways of deriving relation of scaled entrainment depth to ri: stull momentum balance ie plumes decelerate due to bouancy difference and boers energy balance

list of publications where its verified, deardorf, fed, band f. a bit about the disagreement between deardorf and bandf

2.5 Research Goals

The LES studies of Sullivan et al. [19], Federovich et al. [6] and more recently Brooks and Fowler in [3] were carried out on grids of lower resolution than those which began to converge in Sullivan and Patton [18], except for the cases specifically for testing resolution effects. Sullivan and Patton [18] influenced our choice of grid size, in particular within the EL

All of these were carried out on $5 \times 5km$ domains and used a combination of both time and spatial averaging to obtain average profiles. So far, we haven't seen a study involving an ensemble of cases, such that true ensemble averaging can be carried out. We chose this setup to obtain true ensemble averages, and to have a wealth of local points for some basic statistical observations.

Federovich et al. [6] varied their cases by upper lapse rate (γ) over a typical range found in the troposphere IE $1-10K/Km$, whereas Sullivan et al. [19] and Brooks and Fowler in [3] varied surface heat flux and initial inversion ($\Delta\theta$). To obtain a range of Richardson numbers (Ri) we varied both surface heat flux ($w^{'}\theta^{'}$) and upper lapse rate (γ).

2.5.1 Verifying that the Model output is realistic

Since unlike the other LES studies, we initialize with a constant surface heat flux ($\overline{w'\theta'}_s$) working against a constant lapse rate (γ), it would be good to see the formation of a convective boundary layer with the expected average profiles.

Given our concern about a slightly smaller domain than usual, we would like to make sure each of the individual cases are producing coherent turbulent structures and that there is adequate scale separation between the structures with highest energy and the grid size.

Sullivan et al. [19] showed with effective visual aids some of the details of the dynamics in the EL. It would be important to at least confirm our setup is producing comparable motions of warm and cool air in this region.

2.5.2 Local Mixed Layer Heights

The average profiles must correspond to the average of the local profiles. Local potential temperatures are expected to be less smooth and their variance in height corresponds to the depth of the average entrainment layer. Sullivan et al. [19] used a centered differencing gradient method to find the local convective boundary layer (CBL) heights. Brooks and Fowler in [3] apply a wavelet of dilation comparable to EL depth the to local tracer profiles to determine the location of the EL and then a narrower wavelet to determine the limits. Since the local profiles are not smooth, and there is often upper variabilty of similar and greater magnitude than that which separates the mixed layer (ML) from the layer above it the gradient method is not reliable. A typical tracer profile is quite different to a potential temperature profile IE it goes from a large value in the CBL to a much lower value above. So an ideal approximation might be a step function. Usually the variation accross the EL is much greater than any local variation. The vertical potential temperature gradient profile in this study could be approximated by step function but there is variance usually above the EL which is of comparable magnitude to that accross it. So a wavelet technique might not be as well suited. Steyn et al. in [15] fitted an idealized curve to tracer profiles (Lidar backscatter). So we apply this idea and the multi-linear regression method outlined by Vieth in [22] to our local potential temperature profiles. The result is a three line fit, one line for each of the layers IE the ML of almost constant potentia temperature, the EL over which transition to the stable layer above occurs, and the stable layer of constant lapse rate γ. From this the height of the mixed layer (ML) can readily be determined and the distribution of local ML heights (h_0^l) should correspond to the concept of the EL. We would expect increased stability (γ) to reduce the disortion of the inversion interface and so the variation in h_0^l. Increased surface heat flux ($\overline{w'\theta'_s}$)

would increase the overall magnitude of h_0^l so histograms would represent these effects. We would expect also the h_0^l surface to correspond to coherent plumes of warm and cool air. In particular hight h_0^l should correspond to impinging cool plumes at the top of the EL.

2.5.3 Flux Quadrants

Since the average potential temperature profile represents the results of warming, and warming occurrs via the flux of heat from below and above ($\overline{w'\theta'}_s$, $\overline{w'\theta'}_h$) observation and analiysis of the heat flux ($w'\theta'$)s should give some insight as to the shape of vertical average potential temperature profile. For instance is there a clear trend in how the upper lapse rate (γ) influences the extent of downward moving warm air in the the EL and so the heating rate from above of the ML. Quadrant analyses have been carried on the fluxes from both LES output and measurement (Sullivan et al., [19] and Mahrt and Paumier, [10]). The effects of upper lapse rate (γ) on temperature and velocity perturbations in the CBL were analyzed by Sorbjan in [13]. Following these three studies we break the $w'\theta'$ into four quadrants to see the vertical average individual profiles and also the joint distributions at the EL limits and at the inversion (h). In particular to isolate the effects of γ we will scale by the convective velocity and temperature variance scales w^* and $\theta^* = \frac{\overline{w'\theta'}_s}{w^*}$.

2.5.4 Choice of height definitions

Bulk models assume that the region of transition from the ML value to the free atmospheric value in the potential temperature or buoyancy profile corresponds to the region of negative potential temperature or buoyancy flux (Deardorff [4], Federovich et al. [6]). But although the height of maximum average potential temperature gradient or average of local maximum potential temperature gradient used as CBL height (Sullivan et al., [19] and Garcia and Mellado [7]) there does not seem to be an example in the literature where the EL limits are defined in terms of the average potential temperature profile for the purpose of measurement. So here, we test this framework in terms of two scaling relationships, IE define both the CBL height and EL limits in terms of the average vertical potential temperature gradeient. It follows that the temperature jump ($\Delta\theta$) is defined as the difference accross the EL. This is 1st order type definition. An approximation to the zero order definition would be the difference between the ML value and the value at h on the initial temperature profile.

2.5.5 $\frac{w_e}{w^*}$ vs Ri

The relationship of scaled entrainment velocity to Richardson number Ri is well established. (Deardorff [4] Deardorff et al., [5], Stull [17]) and can be reached by first integrtating the reynolds averaged thermodynamic equation, neglecting radiation, and large scale advection, accross the inversion. When the inversion depth is assumed infinitessimly small and there is no turbulence at the upper limit, and the flux at the lower limit is assumed a proportion of the surface flux this becomes

$$w_e \propto \frac{\overline{w'\theta'}}{\Delta\theta} \tag{2.17}$$

and scaling by the convective velocity scale gives, the following

$$\frac{w_e}{w^*} \propto Ri^{-1} \tag{2.18}$$

So this relationship is based on a simplified zero order framework. Strictly the lengthscale and $\Delta\theta$ should be from within this framework. But we will use our 1st order framework definition to test this scaling relationship for all runs. We will compare our $\Delta\theta$ with the zero order approximation and those defined elsewhere in the literature. This may enable comparison with other findings, in regards to this relationship. There is some discussion in the literature about the power exponent of the Richarson number Ri and it seems the two major contenders are -1 and $-\frac{3}{2}$. The latter has been discussed in the context of a shift in entrainment mechanism from eddy turnover to recoil at higher Ri (Turner [21]), under conditions of a large upper lapse rate (γ) Deardorff et al. [5]. Federovich et al. [6] asser that it is inferred when the first order Ri is used IE when the temperature jump accross the EL is used. Whereas Sullivan et al. in [19] speculate a power law other than -1 may apply at lower Ri. We will plot our data in log-log coordinates to observe which if any power law applies to our results.

2.5.6 $\frac{\Delta h}{h}$ vs Ri

Relationship of the scaled EL depth to Richardson number arises from a momentum balance where the depth is considered to be related to the overshoot of the plumes (Stull [16], Deardorff et al. [5]). This in turn is a function of the plumes velocity at the top of the CBL and the buoyancy difference between it and the surrounding stable air. When the velocity at the top is assumed to be proportional the the convective velocity scale (w^*) this becomes

$$\frac{\Delta h}{h} \propto Ri^{-1} \tag{2.19}$$

Boers in [1] arrived at a $-\frac{1}{2}$ power law relationship using an energy balance. IE they equate the difference in potential and thermal energy before and after distortion of the inversion interface to the kinetic energy before distortion. Output and measurements have resulted in power laws ranging from -1 to $-\frac{1}{4}$ (Traumner et al. [20]).

Given that our principal definition of the EL has not been used before we would be happy to see any relationship to Ri. Once we establish there is one, we will use log-log coordinates to see which power law best fits.

Chapter 3

Results

3.1 Description of Runs

All 10 member cases of the ensemble were carried out on a 3.2 x 4.8 Km horizontal domain ($\Delta x = \Delta y = 25m$, $nx = 128$, $ny = 192$). nx, ny were chosen based on the optimal distribution accross processor nodes. The vertical grid ($nz = 312$) was of higher resolution around the entrainment layer (EL) ($\Delta z = 5m$), and lower below and above it ($\Delta z = 10\ to\ 100m$). Grid size was chosen so that a full spectrum of turbulence would be resolved within the EL in line with the findings of Sullivan and Patton in [18]. The 7 runs vary depending on surface heat flux ($\overline{w'\theta'_s}$) and initial lapse rate (γ).

$\overline{w'\theta'_s}$ / γ	10 (K/Km)	5 (K/Km)	2.5 (K/Km)
150 (W/m2)	✓	✓[1]	
100 (W/m2)	✓	✓	
60 (W/m2)	✓	✓	✓

Table 3.1: Runs in terms of $\overline{w'\theta'_s}$ and initial lapse rate γ

[1]Incomplete run: EL exceded high resolution vertical grid after 7 hours

3.2 Relevant Definitions

In large eddy simulation (LES) studies, the CBL height is usually defined as either the point of minimum $\overline{w'\theta'}$ or maximum $\frac{\partial\overline{\theta}}{\partial z}$. A notable exception is the work of Brooks and Fowler in [3] where the authors favoured a statistically based definition using local tracer profiles. Similarly, they define the entrainment layer (EL) in terms of the statistics of local profiles, whereas elsewhere in the literature it is usually defined according to the zero crossings in the vertical $\overline{w'\theta'}$ profile.

Here, the CBL height and EL limits are defined based on the vertical $\frac{\partial\overline{\theta}}{\partial z}$ profile. Namely, the CBL height h is the point where $\frac{\partial\overline{\theta}}{\partial z}$ is maximum, the lower EL limit is the point at which $\frac{\partial\overline{\theta}}{\partial z}$ first increases significantly from zero i.e. exceeds a threshold value above the surface layer, and the upper EL limit h_1 is the point where $\frac{\partial\overline{\theta}}{\partial z}$ resumes γ. (Figure 3.1)

As Brooks and Fowler point out in [3], when using an average vertical tracer profile there is no universal critereon for a significant gradient. So a threshold value for the lower EL limit (h_0) was chosen such that it was positive, small i.e. an order of magnitude less than γ and the same for all runs. For the sake of rigor, the main corresponding result was calculated based on two additional threshold values in Section 4.6.3.

The temperature jump is defined here as the difference in $\overline{\theta}$ accross the EL. So, it is larger than those used by Federovich et al. in [6] to verify their zero order model and Sullivan et al. in [19] (Table 3.2).

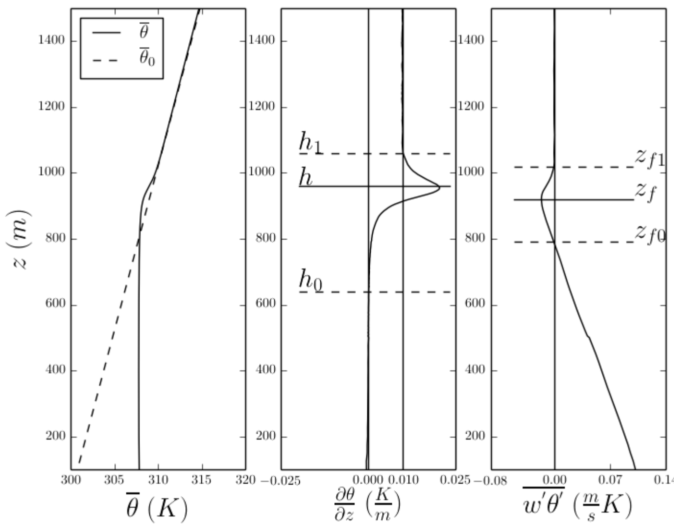

Figure 3.1: Height Definitions

Description	This Study	Sullivan et al. [19]	Fedorovich et al.[6]
CBL Height	$\overline{h_l}$	h	z_f
Temperature Jump	$\Delta\theta = \overline{\theta}(h_1) - \overline{\theta}(h_0)$	$\Delta\theta = \overline{\theta}(z_{f1}) - \overline{\theta}(z_f)$	$\Delta b = b_0(z_f) - b(z_{f0})$
			$\delta b = b(z_{f1})$ - $b(z_{f0})$
Convective Velocity Scale	$w_* = (hB_s)^{\frac{1}{3}}$, $B_s = \frac{g}{\theta_{ML}}\overline{w'\theta'}_s$	$w_* = (hB_s)^{\frac{1}{3}}$, $B_s = \frac{g}{\theta_{ML}}\overline{w'\theta'}_s$	$w_* = (z_f B_s)^{\frac{1}{3}}$
Time Scale	$\tau = \frac{h}{w^*}$	$\tau = \frac{h}{w^*}$	$\tau = N^{-1}$

Table 3.2: Comparison of relevant definitions with those from key publications. $b = \frac{g}{\theta_{ML}}\overline{\theta}$

3.3 Verifying the Model Output

3.3.1 Time till well-mixed

Time must be allowed to establish statistically steady turbulent flow. Sullivan et al. in [19] recommended 10 eddie turnover times based on the convective time scale $\tau = \frac{h}{w^*} = \frac{h}{\left(\frac{gh}{\overline{\theta}_{ML}}(\overline{w'\theta'_s})\right)^{\frac{1}{3}}}$, and Brooks and Fowler in [3] chose a simulated time of 2 hours. For all of the runs, at least 10 eddie turnover times were completed by 2 simulated hours (Figure 3.2). Although each run has a distinct convective velocity scale that increases with time ($w^*(time)$), dividing boundary layer height (h) by it to obtain τ results in a collapse from 7 to 3 curves, one for each γ.

A measureable well mixed layer (ML) and EL based on the horizontaly averaged, ensemble averaged potential temperature ($\overline{\theta}$) profile develops after 2 hours (Figure 3.3). After 2 or 3 hours the EL is fully contained within the vertical region of high resolution.

Averaged heat fluxes ($\overline{w'\theta'}$) (Figure 3.4) and root mean squared vertical velocity perturbations ($\sqrt{w'^2}$) (Figure 3.5) become self similar and are scaled well by the surface heat flux ($\overline{w'\theta'}_s$) and the convective velocity scale (w^*) respectively after 2 hours.

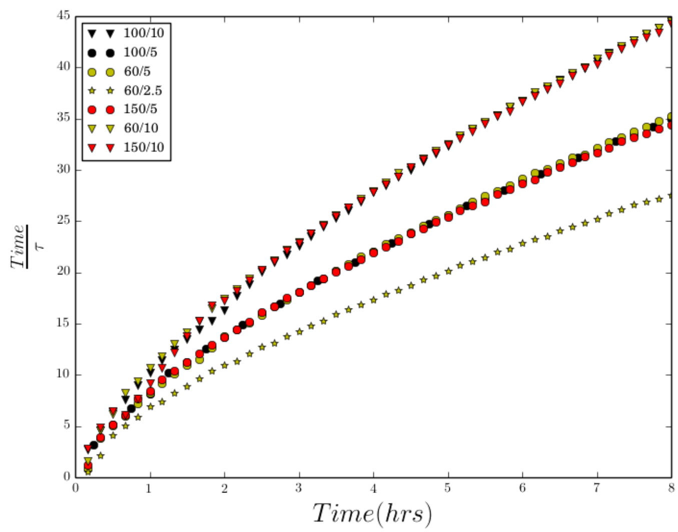

Figure 3.2: Plots of scaled time vs time for all runs. Scaled time is based on the convective time scale and can be thought of as the number of times an eddie has reached the top of the CBL.

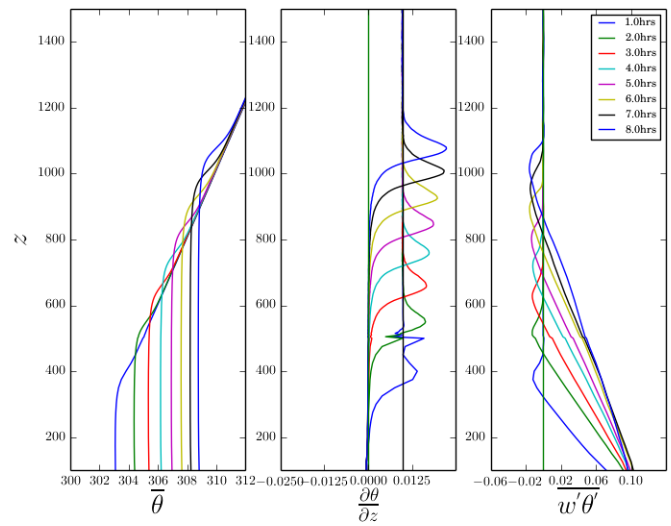

Figure 3.3: Vertical profiles of the ensemble and horizontally averaged potential temperature ($\overline{\theta}$), its vertical gradient ($\frac{\partial\overline{\theta}}{\partial z}$) and heat flux ($\overline{w'\theta'}$) for the 150/10 run

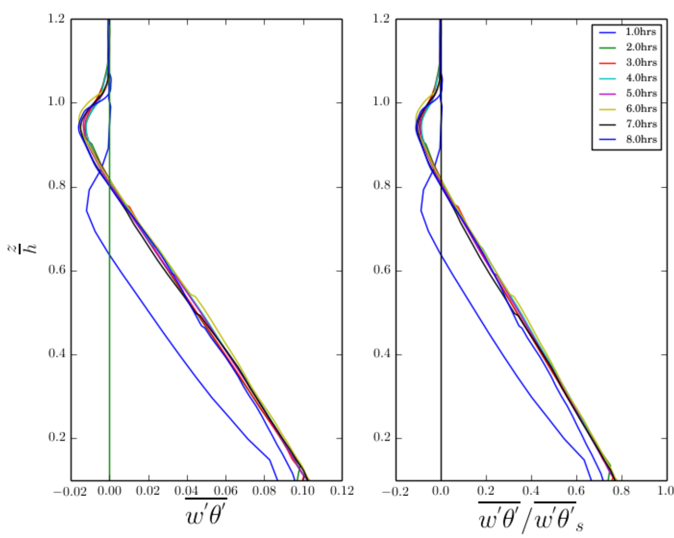

Figure 3.4: $\overline{w'\theta'}$ and scaled $\overline{w'\theta'}$ vs scaled height for the 150/10 run

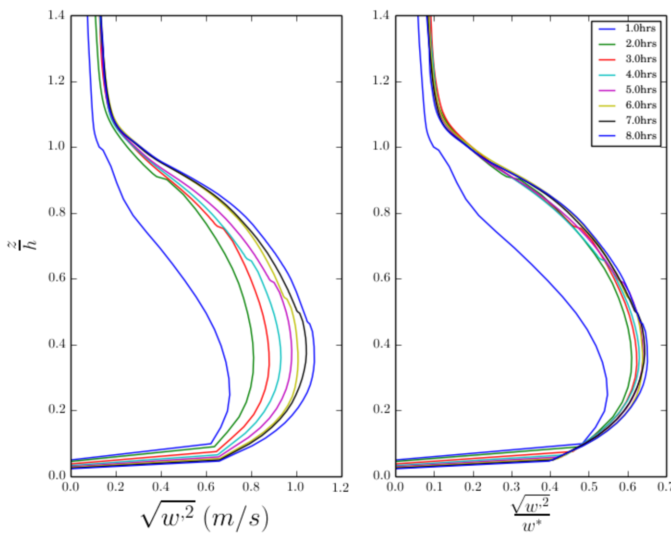

Figure 3.5: $\sqrt{w'^2}$ vs scaled height for the 150/10 run

3.3.2 FFT Energy Spectra

Two dimensional FFT power spectra taken of horizontal slices of $w^{'}$ (Figure 3.6) at three different levels (h_0, h and h_1) are collapsed to one dimension by integrating around a circle of wave-number radius k. Isotropy in all radial directions is assumed and $k = \sqrt{k_x^2 + k_y^2}$.

The resulting scalar density spectra show peaks in energy at the larger scales, cascading to the lower scales roughly according to a $\frac{-5}{3}$ slope, lower in the EL. At the top of the EL where turbulence is supressed by stability, the slope is steeper. The peak in energy occurs at smaller scales at the inversion (h) as compared to at the bottom of the EL (h_0), indicating a change in the size of the dominant turbulent structures further into the entrainment layer (EL).

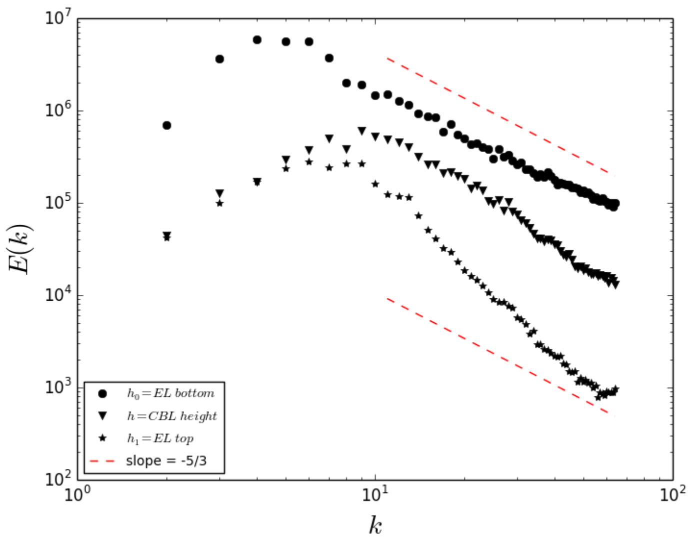

Figure 3.6: Scalar FFT energy vs wavenumber ($k = \sqrt{k_x^2 + k_y^2}$) for the 60/2.5 run at 2 hours. $E(k)$ is $E(k_x, k_y)$ integrated around circles of radius k. $E(k_x, k_y)$ is the total integrated energy over the 2D domain. k_x and k_y are number of waves per domain length.

3.3.3 Ensemble and horizontally averaged vertical Potential Temperature $\overline{\theta}$ and Heat Flux profiles $\overline{w'\theta'}$

The $\overline{\theta}$ profiles exhibit an ML above which $\frac{\partial\overline{\theta}}{\partial z} > 0$ and reaches a maximum value at h before resuming γ at h_1 (Figures 3.3 and 3.7). Convective boundary layer CBL growth is stimulated by $\overline{w'\theta'}_s$ and inhibited by γ.

The horizonally averaged, ensemble averaged heat flux ($\overline{w'\theta'}$) profiles decrease from the surface value ($\overline{w'\theta'_s}$) passing through zero to a minumum before increasing to zero (Figures 3.3 and 3.8). All minima are less in magnitude than the zero order approximation ($-.2 \times \overline{w'\theta'_s}$).

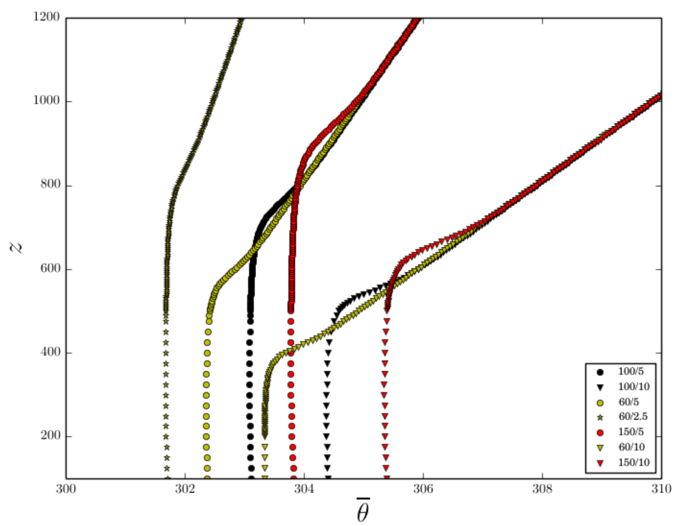

Figure 3.7: $\overline{\theta}$ profiles at 2 hours

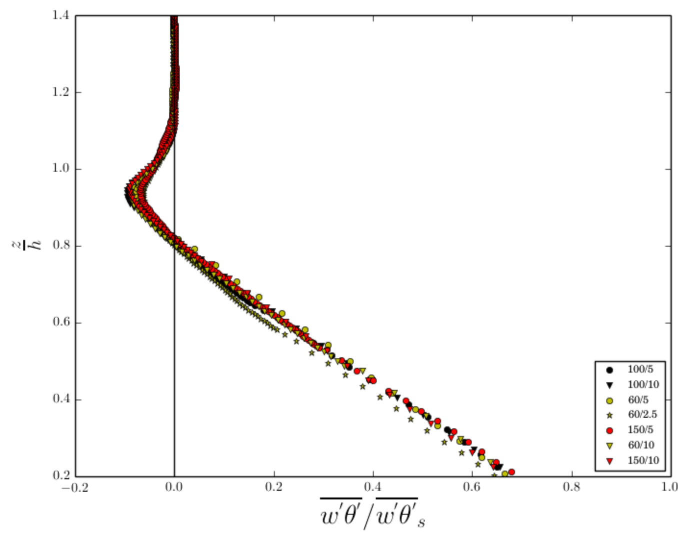

Figure 3.8: Scaled $\overline{w'\theta'}_s$ profiles at 2 hours

3.3.4 Visualization of Structures Within the Entrainment Layer

Horizontal slices, at the three entrainment layer (EL) levels, of the potential temperature and vertical velocity perturbations are plotted to see the turbulent structures. At the bottom of the EL (h_0) in the 150/10 run (Figure 3.9 (a) and (d)) coherent areas of positive and negative temperature perturbations correspond to areas of upward and downward moving air.

The individual plumes of relatively cool air are more evident at the inversion (h) and their locations correspond to areas of upward motion ((b) and (e)). Most of the upward moving cool areas are adjacent to and even encircled by smaller areas of downward moving warm air. At h_1 ((c) and (f)) peaks of cool air are associated with both up and down-welling.

In the 60/2.5 run (Figure 3.10) a similar progression is evident but the impinging, cool upward moving plumes are more defined. This is to be expected since stronger stability inhibits deformation of the inversion interface.

Figure 3.9: θ' (left) and w' (right) at 2 hours at h_0 (a,d), h (c,e) and h_1 (d,f)

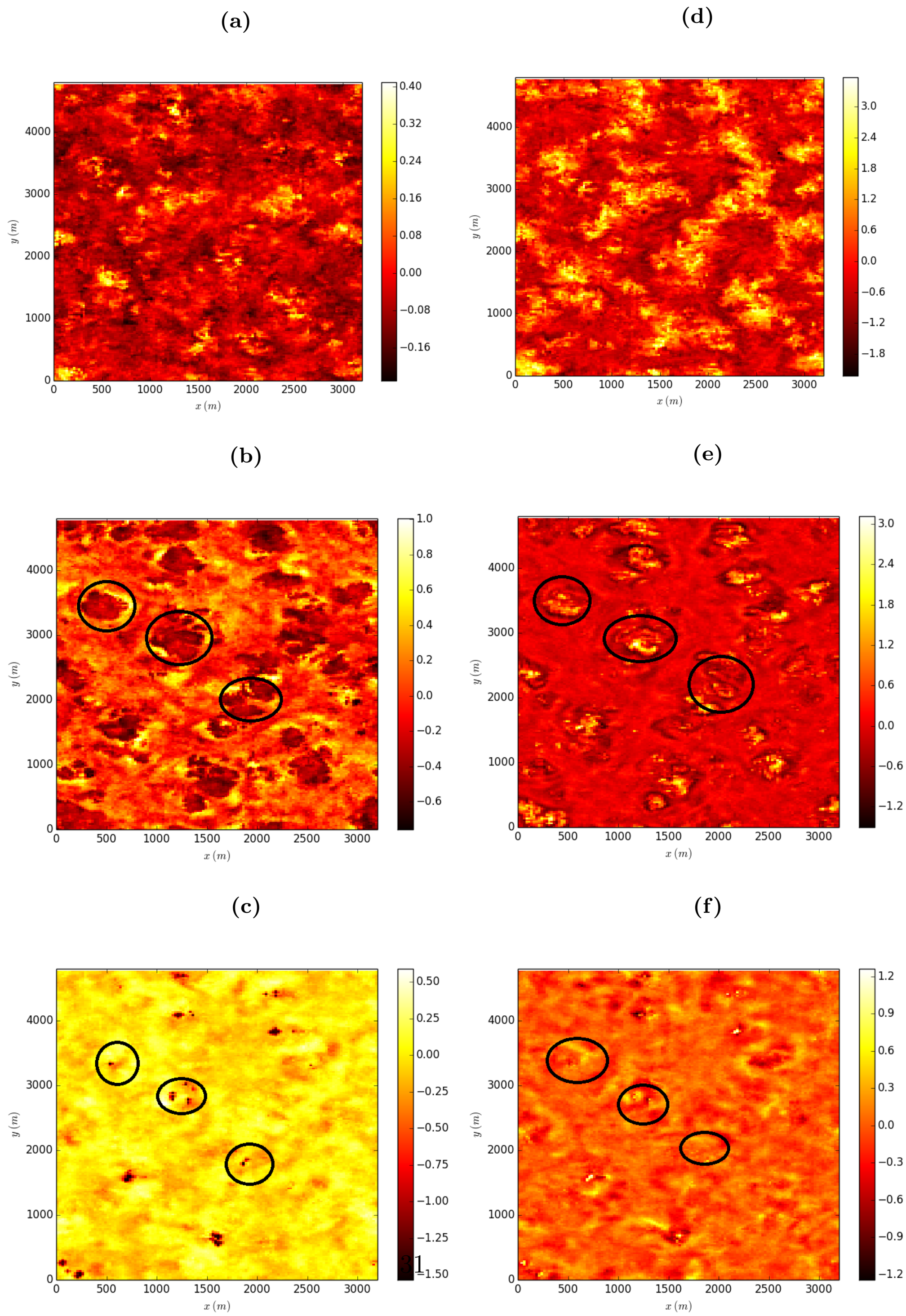

Figure 3.10: θ' (left) and w' (right) at 2 hours at h_0 (a,d), h(b,e) and h_1(c,f)

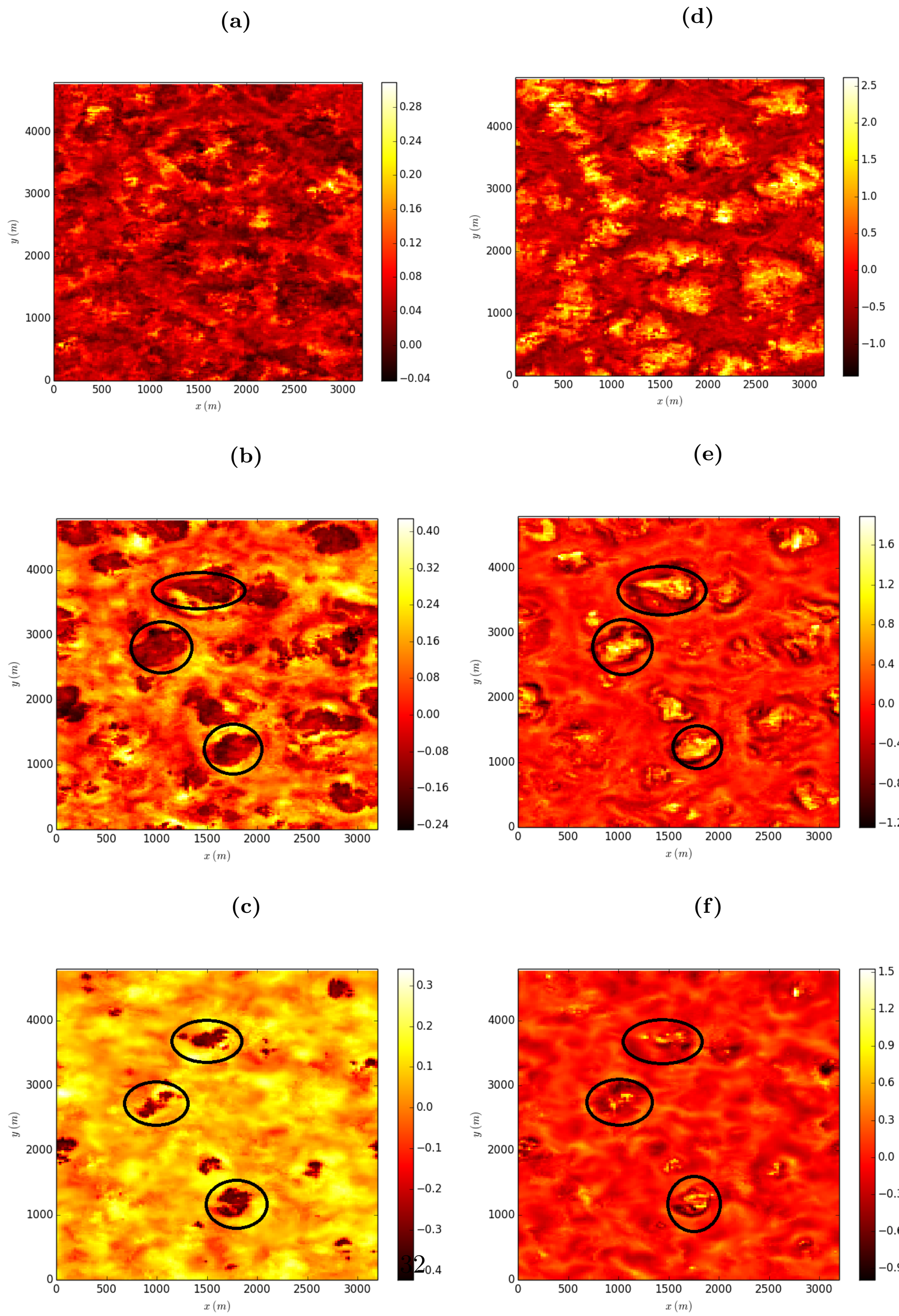

3.4 Local Mixed Layer Heights (h_0^l)

Local θ profiles (Figures 3.11 and 3.12) exhibit a distinct ML before resuming γ but not always a clearly defined EL. There are sharp changes in the profile well into the free atmosphere, due possibly to waves, which render the gradient method for determining h^l unusable. Instead a linear regression method is used, whereby three lines representing: the ML, the EL and the upper lapse rate (γ), are fit to the profile according to the minimum residual sum of squares (RSS). Determining local ML height (h_0^l) was more straight forward than the local height of maximum potential temperature gradient (h^l) for the reasons stated above.

Figure 3.11 shows two local θ profiles where h_0^l is relatively high. A sharp interface is evident indicating that this is within an active plume impinging on the stable layer. In Figure 3.12 where h_0^l is relatively low a less defined interface indicates a point now outside a rising plume. Contour plots (Figure 3.13) show regions of high h_0^l corresponding to regions of upward moving relatively cool air at h.

The distribution of h_0^l is related to the depth of the entrainment layer (EL). Spread increases with increasing $\overline{w'\theta'_s}$ and decreases with increasing γ (Figure 3.14). When scaled by h (Figure 3.15), the local ML height distribution has spread that narrows with increased γ and seems relatively uninfluenced by change in $\overline{w'\theta'}_s$. The upper limit seems to be constant at about $1.1(\times h)$, whereas the lower limit varies depending on γ. Runs with lower h and narrower Δh have relatiively larger spacing between bins and so higher numbers in each bin. The above supports the results outlined in Section 4.6.3.

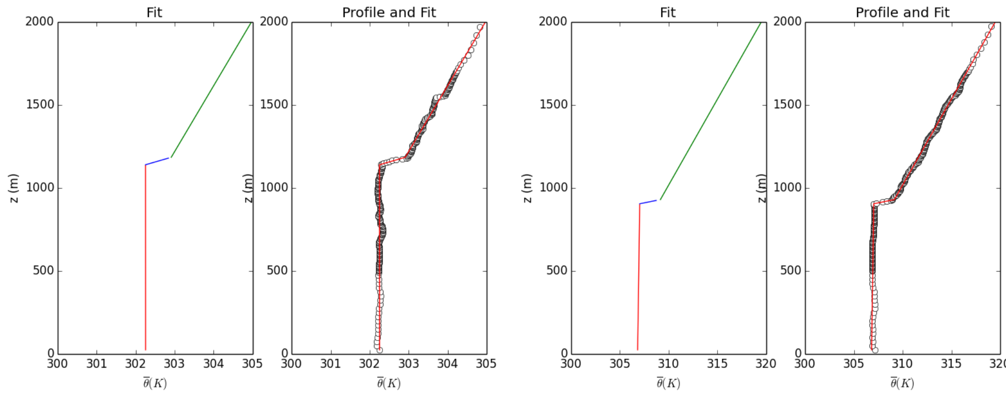

(a) **(b)**

Figure 3.11: Local vertical θ profiles with 3-line fit for the 60/2.5 (a) and 150/10 (b) runs at points where h_0^l is high.

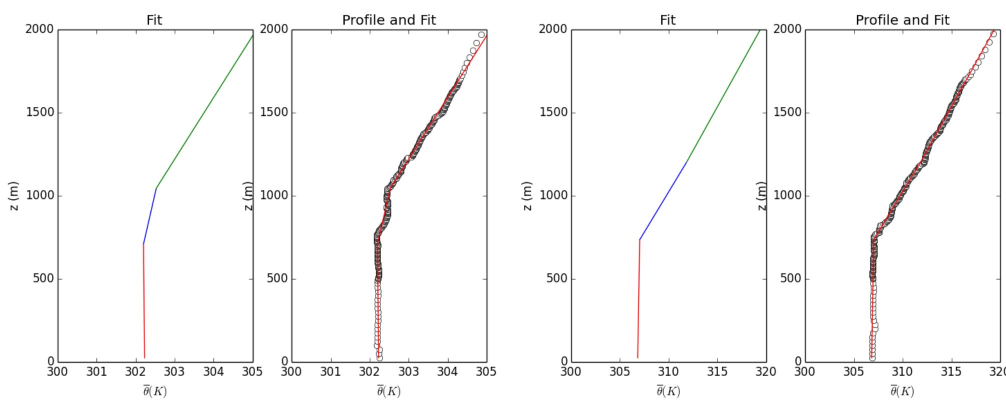

(a) **(b)**

Figure 3.12: Local vertical θ profiles with 3-line fit for the 60/2.5 (a) and 150/10 (b) runs at points where h_0^l is low.

Figure 3.13: θ' (a,d), w'(b,e) at h_1(c,f) and local ML height h_0^l at 2 hours for 60/2.5 (left) and 150/10 (right) runs

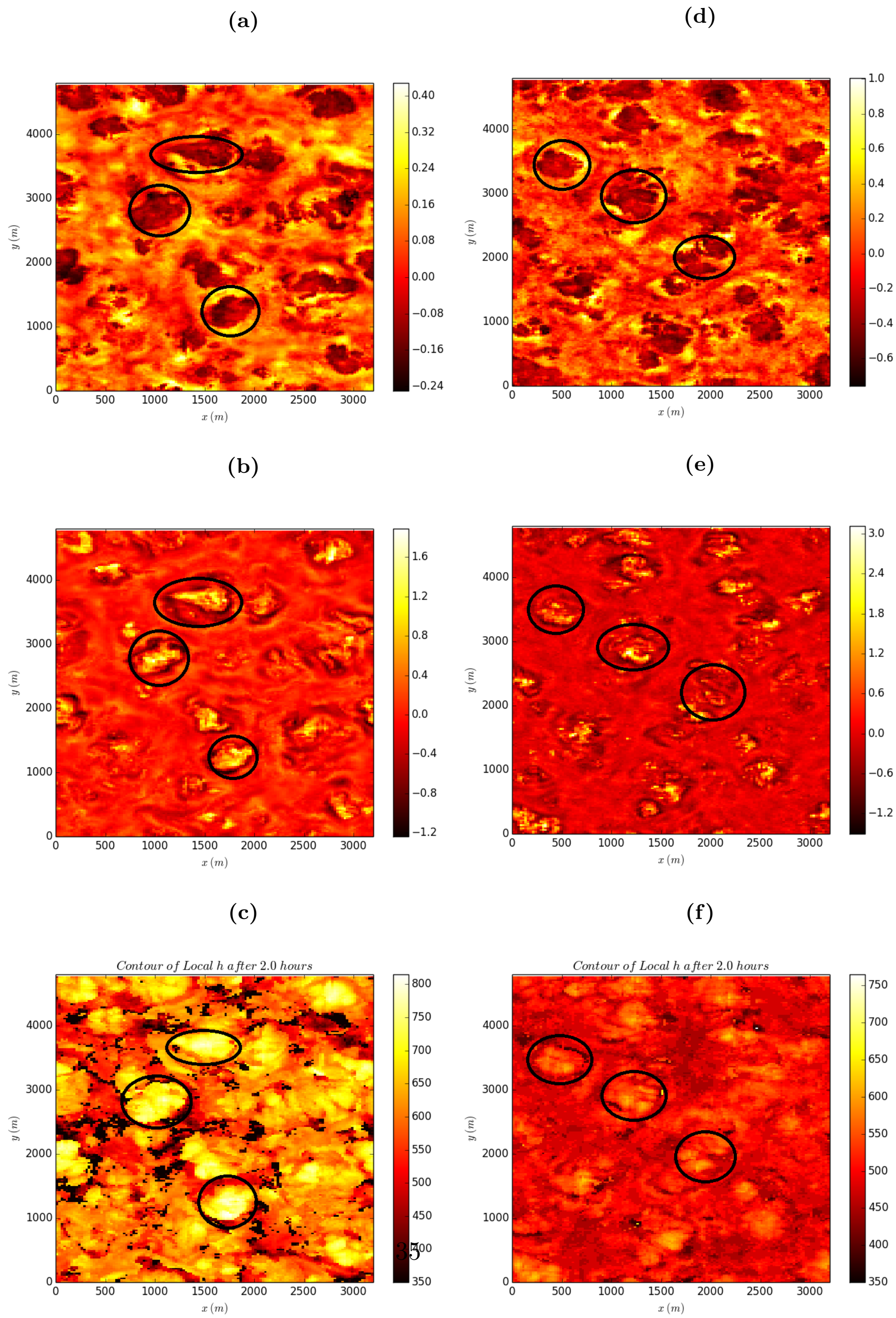

Figure 3.14: Histograms of h_0^l for $\overline{w'\theta'_s} = 150$ to $60(W/m^2)$ (a to c) and $\gamma = 10$ to $2.5(K/Km)$ (c to g) at 5 hours

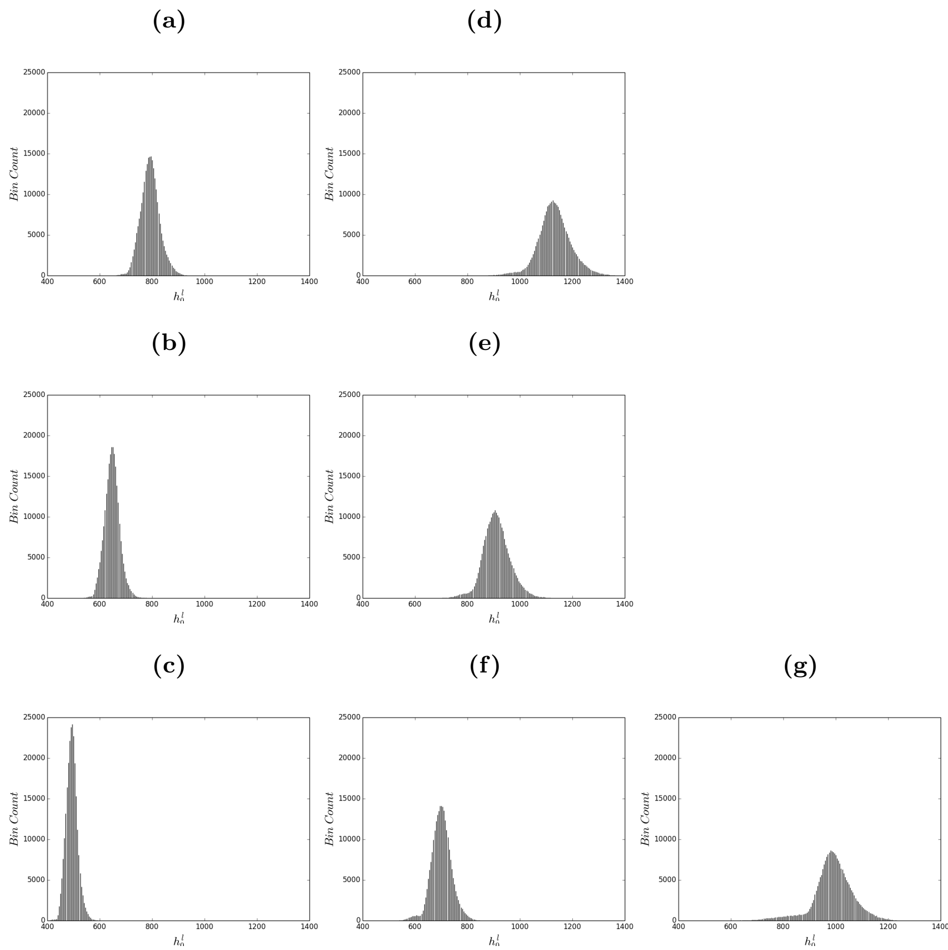

Figure 3.15: PDFs of $\frac{h_0^l}{h}$ for $\overline{w'\theta'_s} = 150$ to $60(W/m^2)$ (a to c) and $\gamma = 10$ to $2.5(K/Km)$ (c to g) at 5 hours

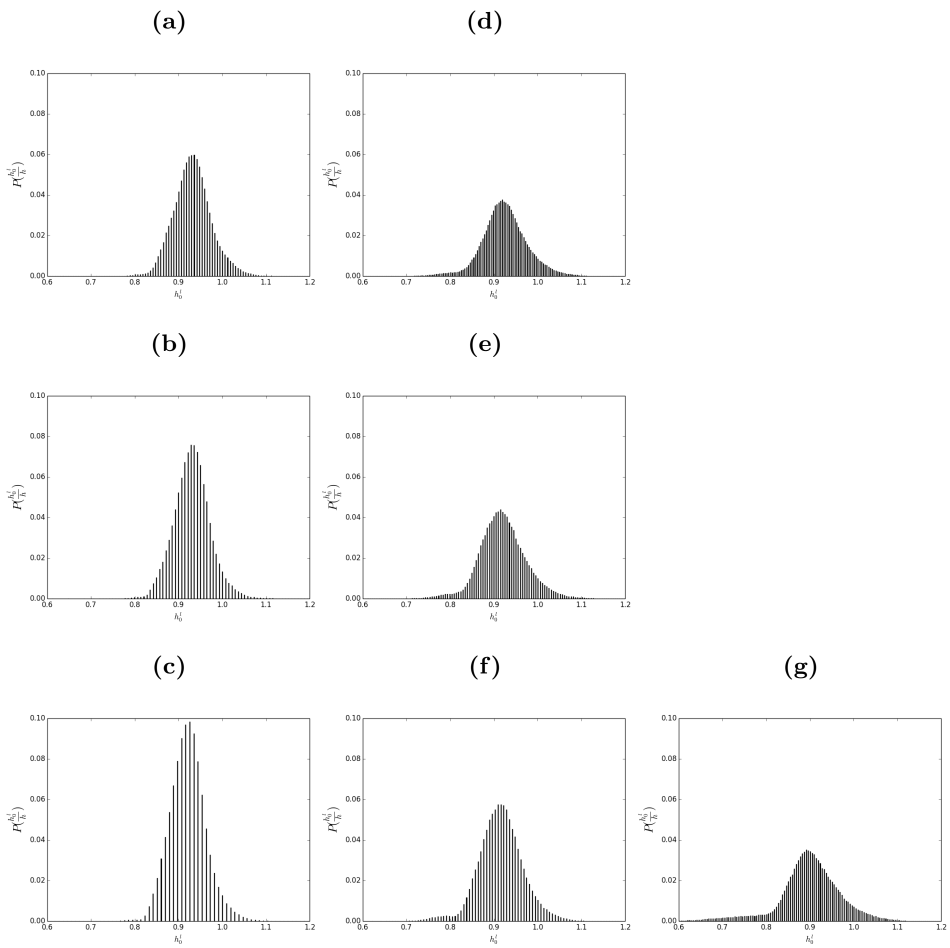

3.5 Flux Quadrants

As Sullivan et al. point out in [19] when broken out into four quadrants (Figure 3.16) the $\overline{w'\theta'}$ profiles have upper extrema above that of the total average profile (z_f). 2D histograms of the four quadrants are plotted at h_0, h and h_1 to see how the distributions are influenced by changes in $\overline{w'\theta'}$ and γ.

At h_0 (Figure **??**) fast updraughts are relatively warm. The spread in $w^{'}$ increases with increasing $\overline{w'\theta'}_s$ and decreases with increased γ. At h (Figure 3.16) the faster updraughts are now relatively cool and movement (both up and down) of warmer air from aloft becomes more prominent. The spread of $w^{'}$ and $\theta^{'}$ both increase with increasing $\overline{w'\theta'}$ whereas that of $\theta^{'}$ increases only slightly with increased stability. As expected stability inhibits both upward and downward $w^{'}$.

Although the quadrant of overall largest magnitude is that of upward moving cool air, Sullivan et al.'s assertion in [19] that in the EL the heat flux is effectively due to downward moving warm air because the other three quadrants cancel, is found to be approximately true. At the top of the EL (Figure 3.19) velocities are damped and the distributions approach symmetry appart from some slow, cool, impinging up- and down-draughts as in Figure 3.13.

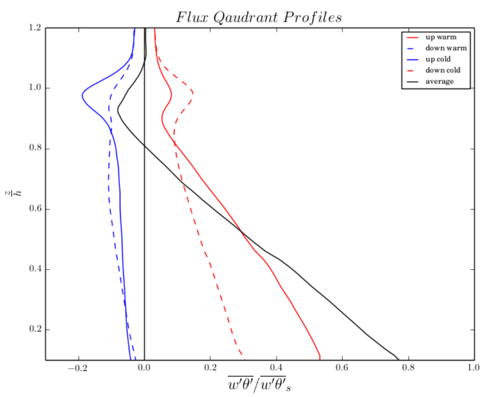

(a)

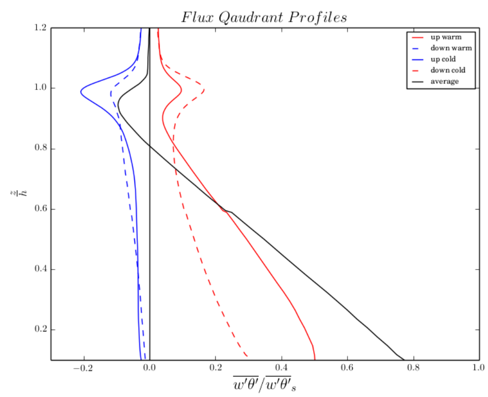

(b)

Figure 3.16: Scaled $\overline{w'\theta'}$ quadrant profiles at 5 hours for the 60/2.5 (a) and 150/10 (b) run

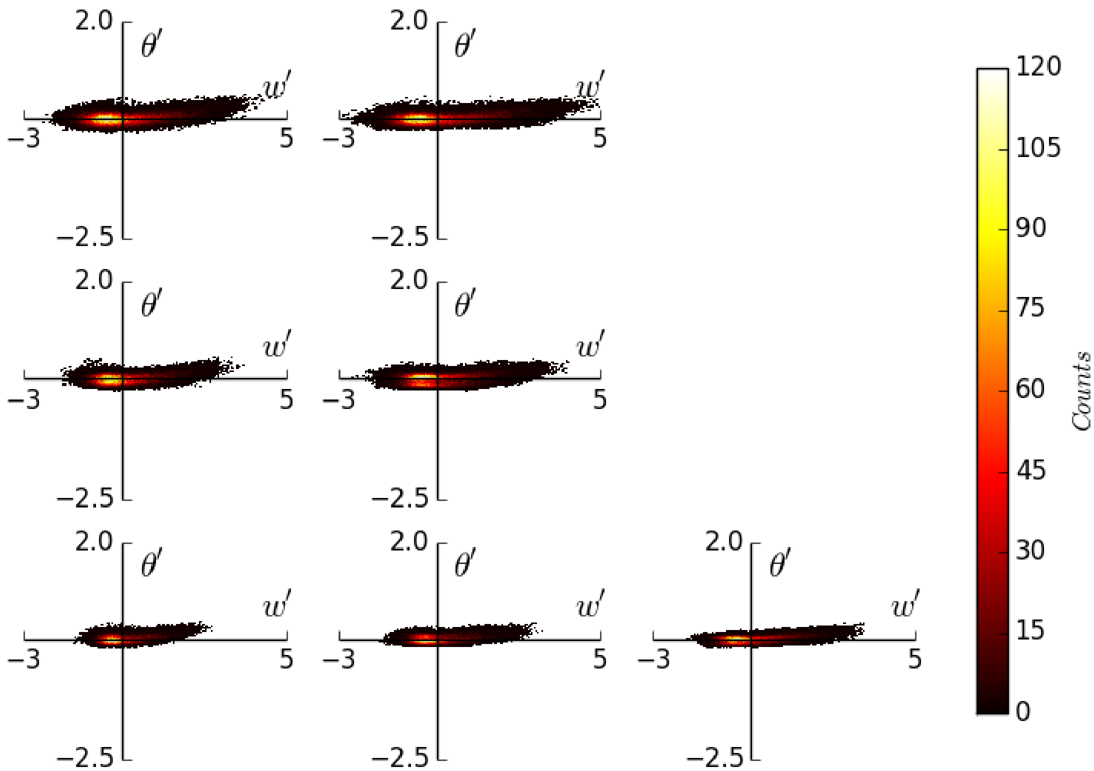

Figure 3.17: $\overline{w'\theta'}$ quadrants at h_0 for $w'\theta' = 150 - 60(W/m^2)$ (top-bottom) and $\gamma = 10 - 2.5(K/Km)$ (left-right) at 5 hours

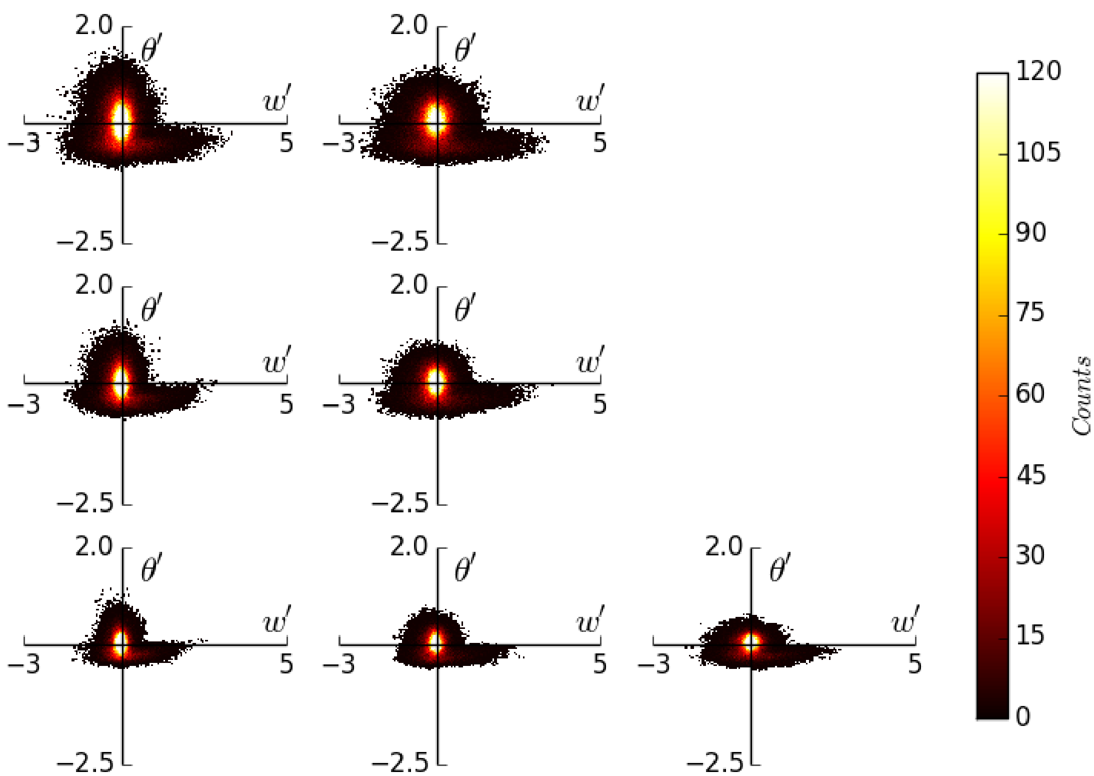

Figure 3.18: $\overline{w'\theta'}$ quadrants at h for $w'\theta' = 150 \ - \ 60(\mathrm{W}/m^2)$ (top - bottom) and $\gamma = 10 \ - \ 2.5(\mathrm{K/Km})$ (left - right) at 5 hours

Figure 3.19: $\overline{w'\theta'}$ quadrants at h_1 for $w'\theta' = 150$ *to* $60(\mathrm{W}/m^2)$ (top to bottom) and $\gamma = 10$ *to* $2.5(\mathrm{K/Km})$ (left to right) at 5 hours

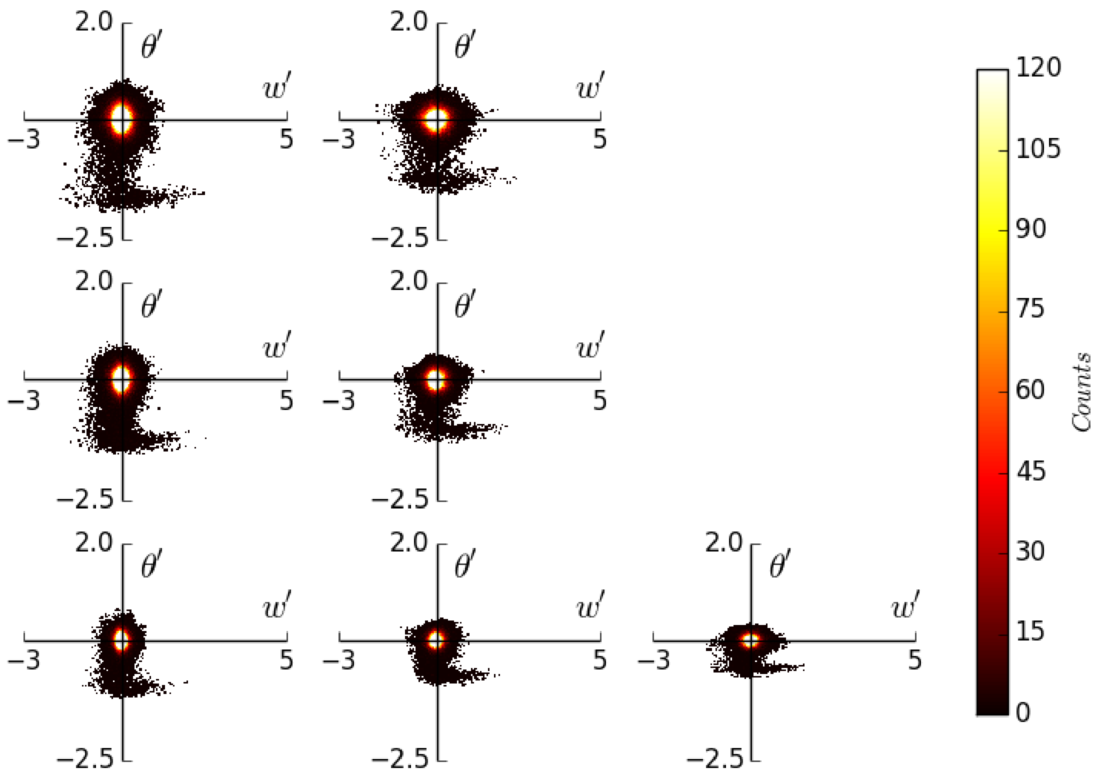

3.6 h and Δh based on Average Profiles

3.6.1 Reminder of Relevant Definitions

Here we define CBL height h as the point at which $\frac{\partial\bar{\theta}}{\partial z}$ is maximum and the EL limits: h_0 the point at which $\frac{\partial\bar{\theta}}{\partial z}$ first exceeds a threshold and h_1 the point at which $\frac{\partial\bar{\theta}}{\partial z}$ resumes γ. The temperature jump $\Delta\theta$ is the difference accross the EL.

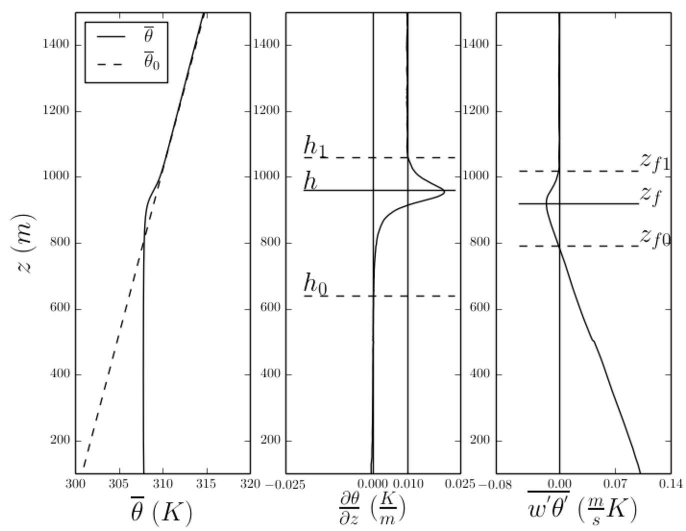

Figure 3.20: Height Definitions

Description	This Study	Sullivan et al. [19]	Fedorovich et al.[6]
CBL Height	h	h	z_f
Temperature Jump	$\Delta\theta = \overline{\theta}(h_1) - \overline{\theta}(h_0)$	$\Delta\theta = \overline{\theta}(z_{f1}) - \overline{\theta}(z_f)$	$\Delta b = b_0(z_f) - b(z_f)$
			$\delta b = b(z_{f1})$ - $b(z_{f0})$
Convective Velocity Scale	$w_* = (hB_s)^{\frac{1}{3}}$, $B_s = \frac{g}{\theta_{ML}}\overline{w'\theta'}_s$	$w_* = (hB_s)^{\frac{1}{3}}$, $B_s = \frac{g}{\theta_{ML}}\overline{w'\theta'}_s$	$w_* = (z_f B_s)^{\frac{1}{3}}$
Richardson Number	$Ri = \frac{\Delta\theta h}{w^{*2}}$	$Ri = \frac{\Delta\theta h}{w^{*2}}$	$Ri_{\Delta b} = \frac{\Delta b z_f}{w^{*2}}$, $Ri_{\delta b} = \frac{\delta b_i z_f}{w^{*2}}$

Table 3.3: Comparison of relevant definitions with those from key publications

3.6.2 $\frac{w_e}{w^*}$ vs Ri^{-1}

Covective Boundary Layer (CBL) height (h) (Figure 3.21) grows rapidly initially with a steadily decreasing rate and relates to the square root of time (Figure3.22). It is found to be proportionate to the height of minimum flux (z_f) (Figure 3.23).

Inverse Richardson Number (Ri^{-1}) decreases with respect to time and clusters according to γ. (Figure 3.24). The entrainment rate ($w_e = \frac{dh}{dt}$) is determined from the slope of a second order polynomial fit to $h(time)$ (Figure 3.21). When scaled by (w^*) it is a roughly linear function of Ri^{-1} (Figure 3.25).

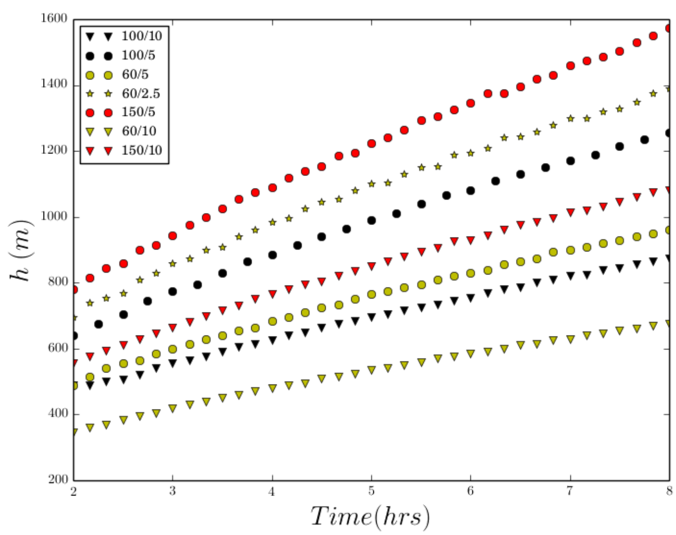

Figure 3.21: h vs time for all runs

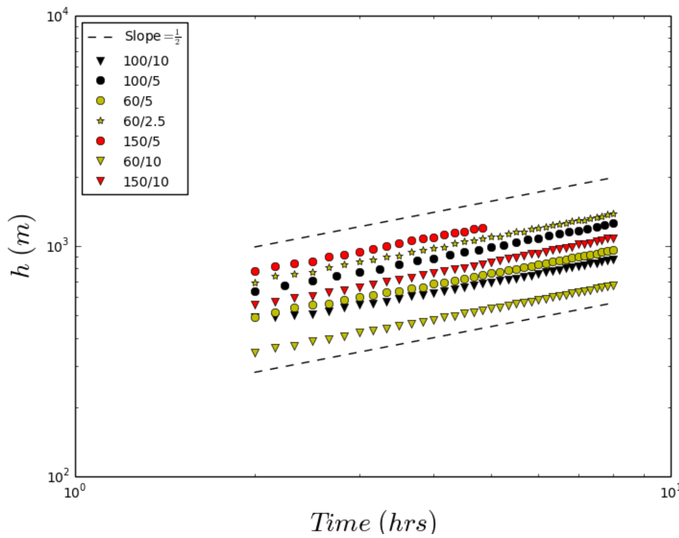

Figure 3.22: Log-Log plot of h vs time for all runs

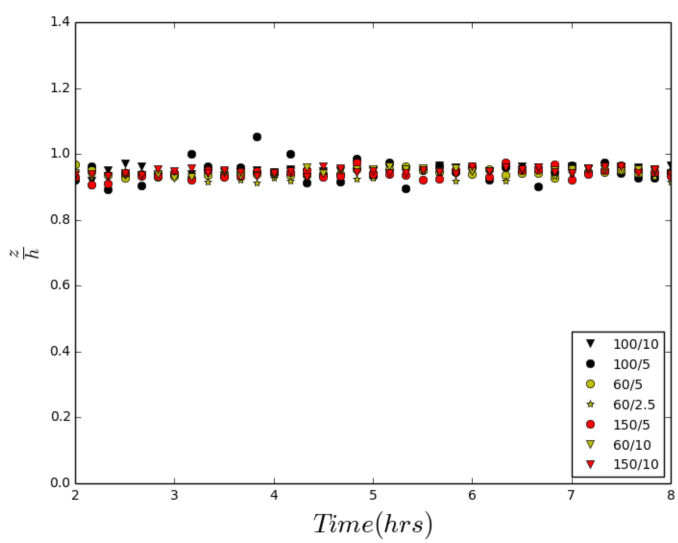

Figure 3.23: $\frac{z_f}{h}$ vs Time

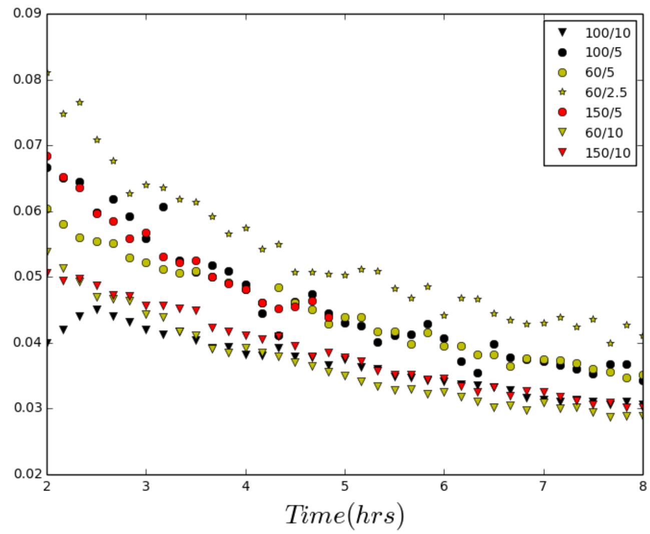

Figure 3.24: Inverse bulk Richardson Number vs time

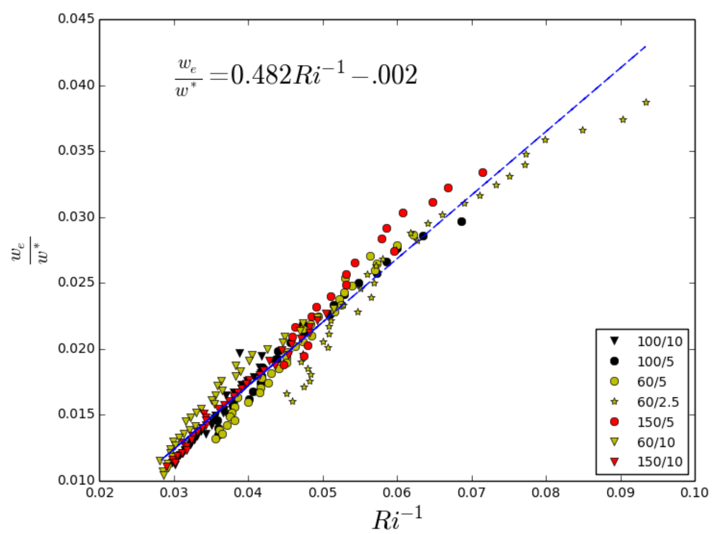

Figure 3.25: Scaled Entrainment rate vs inverse Richardson Number (Ri)

3.6.3 $\frac{\Delta h}{h}$ vs Ri^{-1}

The scaled upper EL limits ($\frac{h_1}{h}$) collapse well in Figure 3.26 to an initial value of approximately 1.15, decreasing to about 1.1. $\frac{h_0}{h}$s appear grouped according to γ and increase with respect to time. So overall the scaled EL appears to narrow with time. The scaled flux based EL (z_{f0} and z_{f1}) appears to remain constant with respect to time in Figure 3.27.

The lower entrainment layer limit h_0 is the point at which the vertical $\frac{\partial \overline{\theta}}{\partial z}$ exceeds a threshold (.0002) chosen such that it is positive, and at least an order of magnitude smaller than γ. Although the resulting scaled EL depth decreases with increasing Ri grouping according to γ is evident in Figure 3.29.

To explore how varying the threshold value affects the relationship between scaled EL depth and Richardson number (Ri), plots analogous to Figure 3.29 were produced at two additional thresholds. A higher threshold value (.0004) results in a higher h_0 (Figure 3.30) and so a narrower EL but a similar grouping according to γ (Figure3.31). A lower threshold value (.0001) results in a lower h_0 (Figure 3.32) but also similar grouping according to γ (Figure 3.33.

When the height definitions are based on the scaled vertical $\frac{\partial \overline{\theta}}{\partial z}$ i.e. $\frac{\partial \overline{\theta}}{\partial z}/\gamma$ profile, only h_0 changes and for clarity we call this EL depth Δh^* and the revised Richardson number Ri*. The curves now collapse and scaled EL depth is seen to decrease with increasing Ri* (Figures 3.34 to 3.36).

There is a slight collapsing effect on the scaled entrainment rate vs Ri relationship when the heights are defined based on the scaled vertical potential temperature gradient $\frac{\partial \overline{\theta}}{\partial z}/\gamma$ profile in Figure 3.37.

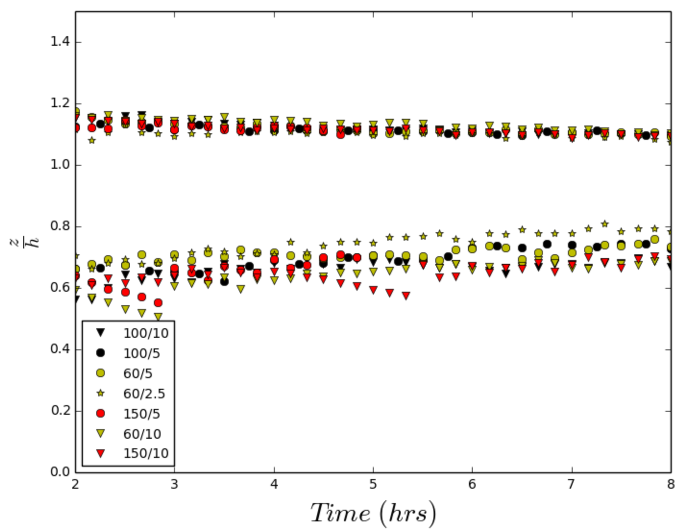

Figure 3.26: Scaled Entrainment Layer limits ($\frac{h_1}{h}$ and $\frac{h_0}{h}$) vs time

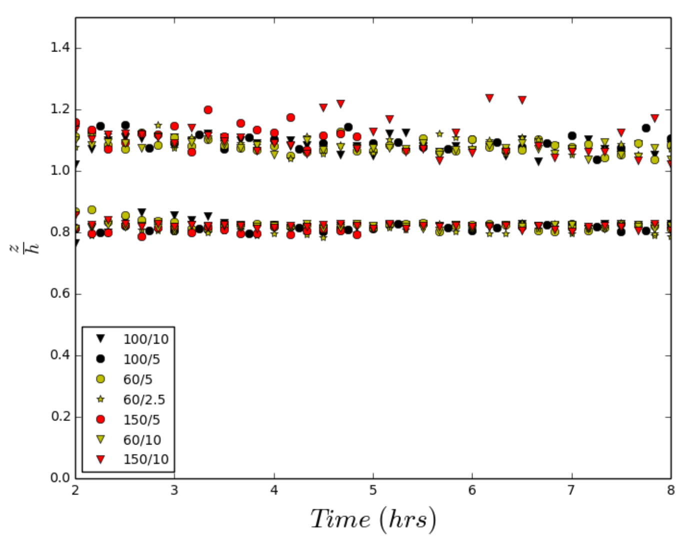

Figure 3.27: Scaled Entrainment Layer limits (z_{f1} and z_{f0}) vs time

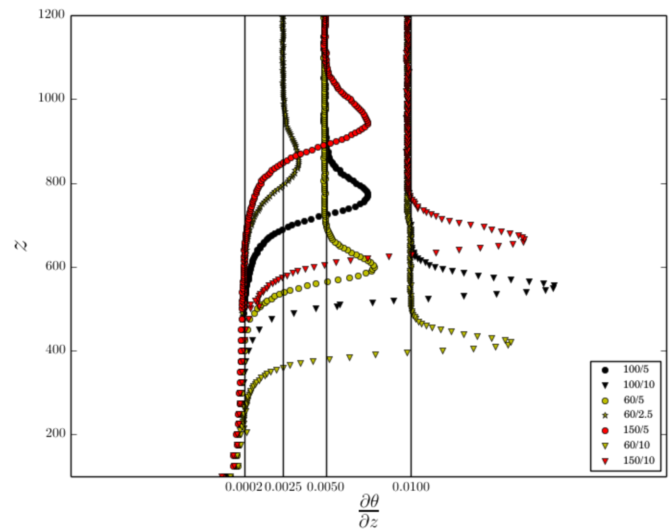

Figure 3.28: Vertical $\frac{\partial\overline{\theta}}{\partial z}$ profiles with threshold at .0002

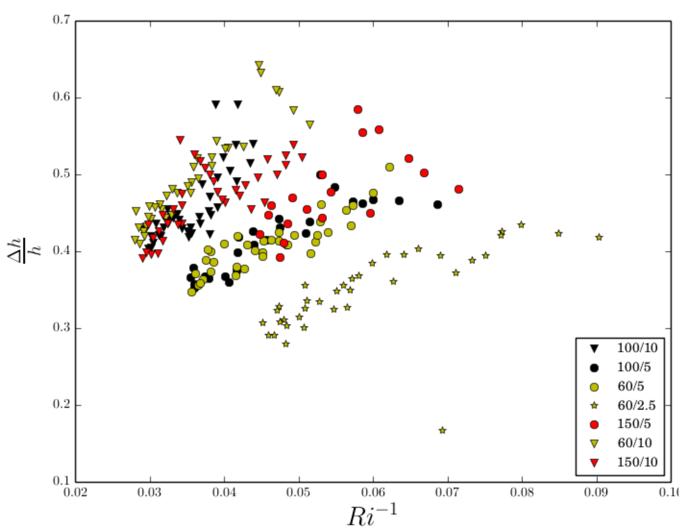

Figure 3.29: Scaled EL depth vs inverse bulk Richardson Number with threshold at .0002

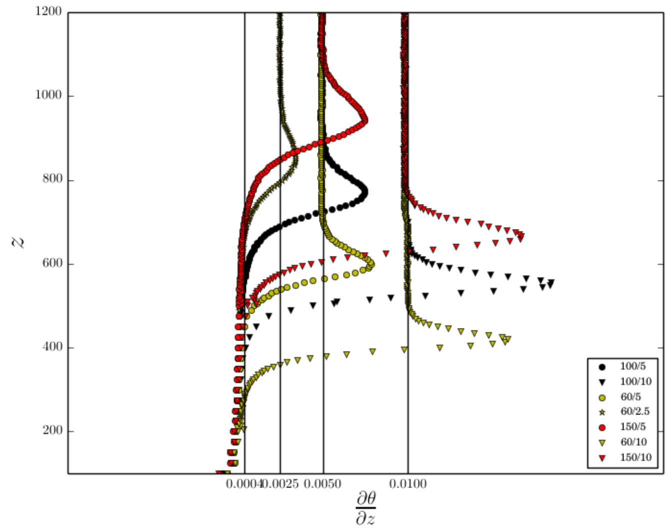

Figure 3.30: Vertical $\frac{\partial\bar{\theta}}{\partial z}$ profiles with threshold at .0004

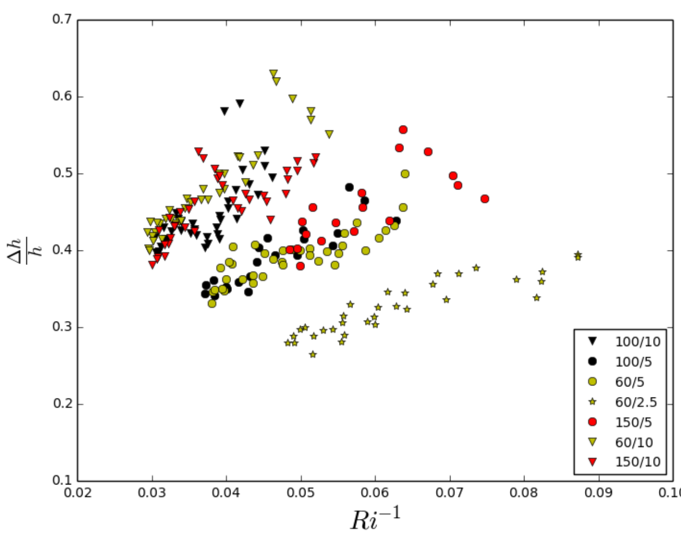

Figure 3.31: Scaled EL depth vs inverse Richardson Number with threshold at .0004

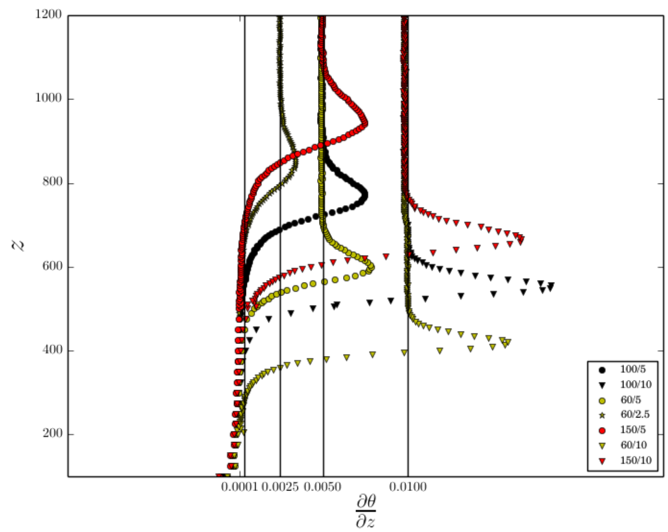

Figure 3.32: Vertical $\frac{\partial\overline{\theta}}{\partial z}$ profiles with threshold at .0001

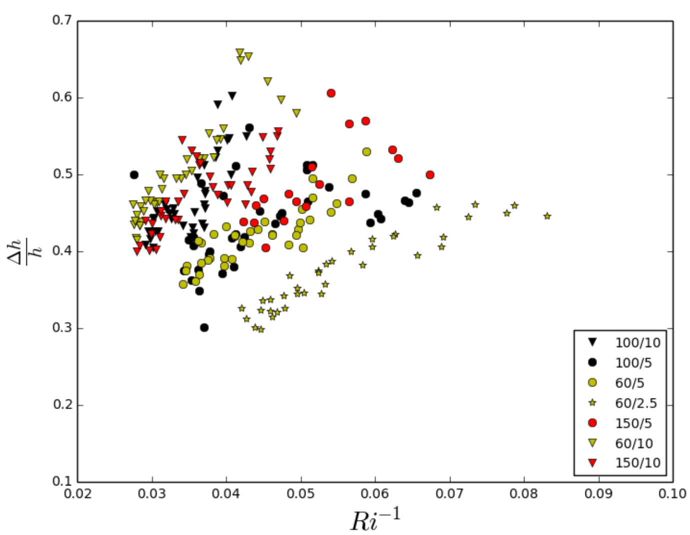

Figure 3.33: Scaled EL depth vs inverse bulk Richardson Number with threshold at .0001

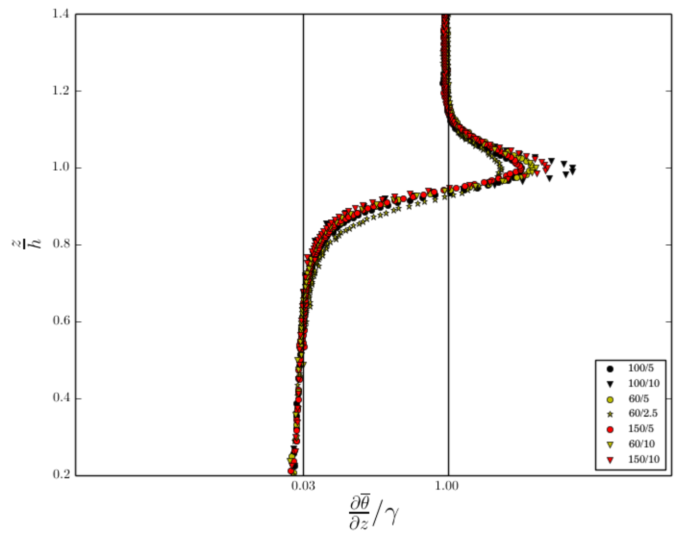

Figure 3.34: Scaled vertical $\frac{\partial\overline{\theta}}{\partial z}$ profiles with threshold at .03

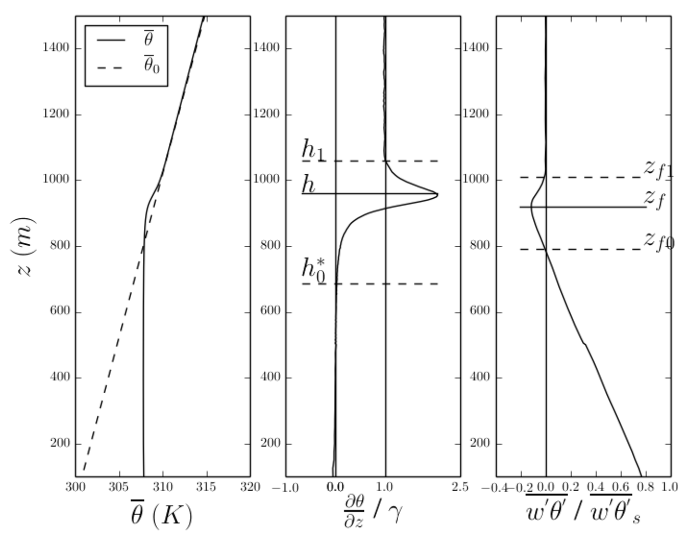

Figure 3.35: Revised height definitions based on scaled $\frac{\partial\overline{\theta}}{\partial z}$ profiles with threshold at .03

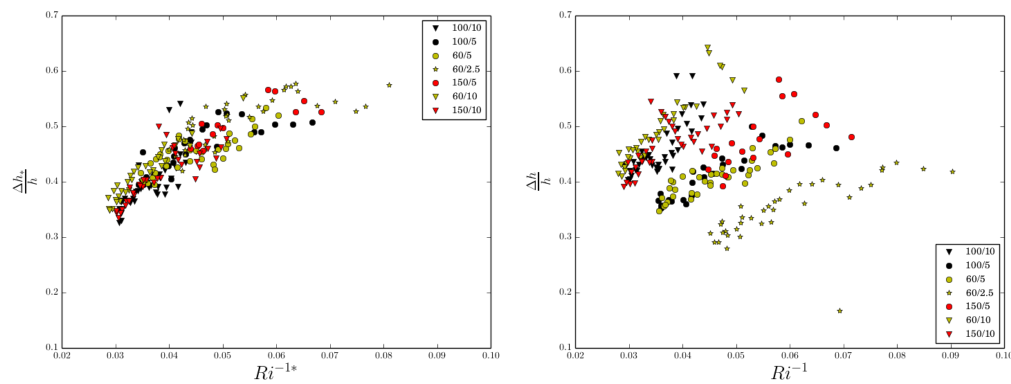

(a) **(b)**

Figure 3.36: Scaled EL Depths vs inverse bulk Richardson number based on scaled $\frac{\partial\overline{\theta}}{\partial z}$ (a) and $\frac{\partial\overline{\theta}}{\partial z}$ (b)

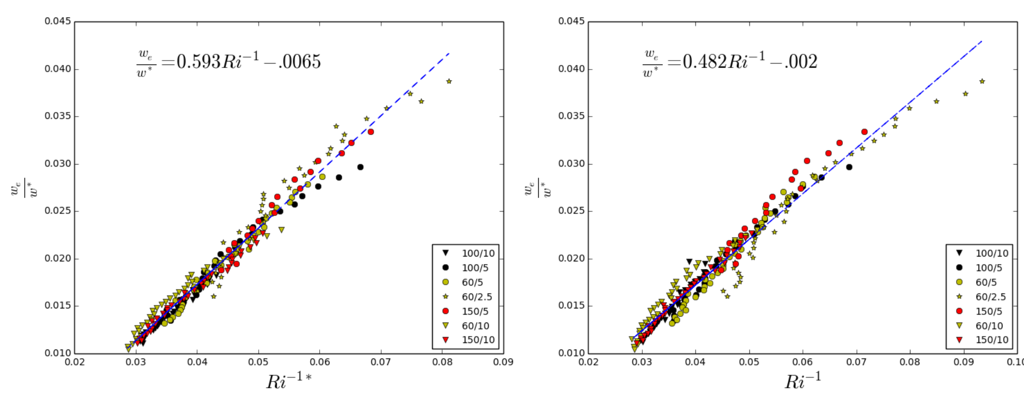

(a) **(b)**

Figure 3.37: Scaled Entrainment Rate vs inverse bulk Richardson number based on scaled $\frac{\partial\overline{\theta}}{\partial z}$ (a) and $\frac{\partial\overline{\theta}}{\partial z}$ (b)

Chapter 4

discussion

4.1 Description of Runs

The domain for each individual case is small relative to that used by Sullivan et al. in [19], Federovich et al. in [6] and Brooks and Fowler in [3] i.e. $5Km \times 5Km$ in the horizontal. Sullivan et al. ([19]) did a higher resolution run on a $3Km \times 3Km$ horizontal domain and noticed a higher convective boundary layer height (h) but similar slope in h with respect to scaled time when compared with the analogous run on a larger domain with lower resolution. They speculated the smaller domain enforced a smaller limit on plume size, thus influencing h. But according to Sullivan and Patton ([18]) grid size also impacts h.

Sullivan et al.'s ([19]) grid spacing for most of their runs was $\Delta x, y = 33.3$, $\Delta z = 10$ except for the run on the smaller domain which had $\Delta x, y = 15$, $\Delta z = 6.67$. The highest resolution Federovich et al. used in [6] was $\Delta x, y = 50$ and $\Delta z = 20$. Brooks and Fowler in [3] used $\Delta x, y = 50$ and $\Delta z = 12$ except in resolution test runs where they used $\Delta x, y = 25$ and $\Delta z = 7.27$. So the vertical resolution around the entrainment region in this study ($\Delta z = 5m$) is higher that the other LES studies. Both Sullivan et al. ([19]) and Brooks and Fowler ([3]) use varying grids in the vertical, such that the region around the entrainment layer (EL) is of higher resolution than elsewhere. We do the same in this study and noticed slight kinks in some of the profiles where the transition to and form higher resolution occurs. We will perform one run on a uniform vertical grid at $\Delta z = 5m$ to verify that this does not effect the results.

Sullivan et al.'s ([19]) initialized with a layer of constant potential temperature topped by an inversion topped by a constant lapse rate ($\gamma \approx 2.5K/Km$). They applied constant average surface heat fluxes ($\overline{w'\theta'}_s$) ranging from about $20-450\ Watts/m^2$. Brooks and Fowler ([3]) followed suit, in that their range of Richardson numbers (Ri) resulted from variation of initial inversion ($\Delta\theta$) strength and average surface heat flux ($\overline{w'\theta'}_s$). Federovich et al. in [6] start with a finite layer of constant average potential temperature ($\overline{\theta}$) above which there was a constant lapse rate which they varied from $1-10\ K/Km$. In this study we begin with a constant $\overline{w'\theta'}_s$ acting against uniform potential temperature lapse rate. Schmidt and Schumann point out in [12] that as a convectively mixed layer (ML) grows against a stable lapse rate (γ) overshoot of the plumes to buoyancy levels above their own, and subsequent entrainment causes a sharp temperature gradient. (see Table 3.1)

4.2 Relevant Definitions

See Table 3.2.

Sullivan et al. ([19]) compared four methods of determining CBL height, two of which they based on the vertical average heat flux ($\overline{w'\theta'}$) profile. For both, the time-series were a lotless smooth than that for z_f determined in this study. Their gradient and contour methods produced smoother time-series plots. The former, they determined from the horizontal average of the local heights of maximum vertical potential temperature gradient. Description of the contour method will be omitted since it is not directly useful. Their gradient based height is consistently higher than the heat flux based definitions i.e. the flux based definition overall is about 0.9 times the gradient definition. This is in line with the findings of this study. They did not focus on EL depth. For their Richardson number (Ri) they calculated $\Delta\theta = \overline{\theta}(z_{f1}) - \overline{\theta}(z_f)$. This value is likely to be smaller than, and not necessarily proportionally to the $\Delta\theta$ used in this study.

Federovich et al. in [6] determined CBL height and EL depth from the horizontal and time ($100 \times 2s$) averaged vertical $\overline{w'\theta'}$ profiles. They used two difference buoyancy ($\frac{g\overline{\theta}}{\theta_{ML}}$) jumps: $\Delta b = \overline{\theta}_0 z_f - \overline{\theta} z_{f0}$ for comparison with the zero order model and $\delta\theta = \overline{\theta} z_{f1} - \overline{\theta} z_{f0}$ for comparison with the first order model and analysis of the EL.

Brooks and Fowler ([3]) used tracer concentration profiles and compare a number of different corresponding CBL height definitions. Although their height and temperature jump used to calculate the Richardson number (Ri) are quite different, their scaling relations based on the fluxed based definitions can be compared to those in this study. For example the corresponding scaled entrainment rate vs Ri plot has a lotof scatter.

The definitions that perform best in relation to Ri for Brooks and Fowler ([3]) are those based on the means of locally determined heights. That based on the domain averaged tracer profile, ie the point of maximum vertical gradient, is directly comparable to our h. Although, this last definition does not produce a plot as correlated as ours.

Their scaled statistical EL definitions based on the local vertical gradient and the local wavelet covariance decrease with increasing Ri similarly to ours, but their flux based definition ($2 \times (z_{f1} - z_f)$) show slight and opposite trends when averaged differently. The latter is in line with what we found.

The height definitions in this study are all based on the average vertical potential temperature gradient ($\overline{\theta}$). It seems to be assumed that the region, where the average potential temperature increases significantly from its mixed layer (ML) value through the maximum to that of the free atmosphere, corresponds to the EL as enclosed by the zero levels in the average potential temperature flux profiles (Deardorff [4], Federovich et al. [6], Garcia and Mellado [7]). But the average potential temperature profile is not used to quantitatively define the EL.

Brooks and Fowler ([3]) discuss the draw-backs of defining the EL based on the gradient of an average tracer profile. Specifically the inconsistency in the size of the gradient relative to a maximum, at the average EL limits as defined based on the local limits. They found the relative size had significant scatter and varied according to Ri. Their maximum and the manner in which they determine is not reproducible in our framework but their conclusion could serve as a caution.

Since in the ML on average there is a gradual increase through zero in average potential temperature above the surface layer, rather than a region where the gradient is zero. So a threshold value must be chosen to identify the lower limit of the EL. This threshold should be less than the upper lapse rate (γ), positive and consistent for all runs. It was chosen by looking at the gradient profile and selecting a point which looked reasonable. The principal result was plotted at three different thresholds based on the unscaled gradient ($\frac{\partial\overline{\theta}}{\partial z}$) profiles.

The upper EL limit is defined as the point at which the average vertical potential temperature gradient resumes γ. These two limits then represent: the point above the surface layer at which the air on average begins to be less turbulently mixed, and the lowest point at which the air is unaffected as yet by the convected turbulence. Our principal length scale h is the point at which the gradient is maximum i.e. the point at which on average the air differs greatest from that directly above it. Our $\Delta\theta$ is the difference in average potential temperature ($\overline{\theta}$) over the EL. We compare h with the fluxed based definitions.

4.3 Verifying the Model Output

4.3.1 Time till well-mixed

To establish statistically steady turbulent flow Sullivan et al. in [19] ran from the same random initial conditions on their coarse grid for more than ten eddy turnover times. Then they switched on the nested high resolution grid and continued for another 4 Odie turnovers. Brooks and Fowler ([3]) waited 2 simulated hours before they judged the turbulence to be fully developed. To initialize turbulence they added a small random perturbation to the temperature field.

Federovich et al. ([6]) focus on the attainment of a quasi-steady state regime within which their zero order entrainment equation holds. Their derivation also hinges upon parametrizations for turbulent kinetic energy (e) and dissipation (ϵ):

$$e = w^{*2}\Psi_e\left(\frac{z}{z_i}\right) \;\; \epsilon = \frac{w^{*3}}{z_i}\Psi_\epsilon\left(\frac{z}{z_i}\right) \tag{4.1}$$

Where the two functions of dimensionless height integrate over the CBL to constants, for example

$$\int_0^{z_i} \frac{e}{w^{*2}} dz = C_e \tag{4.2}$$

In the referenced regime, CBL growth is much slower than the convective velocity scale (w^*), there is a constant entrainment ratio $-\frac{\overline{w'\theta'}_{min}}{\overline{w'\theta'}_s}$ and change in the total e and it's escape from the boundary layer through waves are negligible relative to the buoyant production and dissipation rate. The resulting entrainment equation predicts a $\frac{1}{2}$ power law relationship between the normalized height, $z_i B_s^{-\frac{1}{2}} N^{\frac{3}{2}}$ and time tN. Since variation in $\overline{\theta}$ results in less than 3 percent variation in N, when the surface heat flux B_s and γ are constant this roughly translates to a $\frac{1}{2}$ power law relationship between h and time. In our study we find this to be the case (see Figure 3.23).

We also observe self similarity of the scaled flux profiles, and so a constant entrainment ratio (see Figure 3.4). By 2 hours of simulated time, at least 10 eddy turnover times have elapsed and by 3 hours the EL is fully within the region of high vertical resolution. Worth noting is the collapse in scaled time curves from 7 to 3 according to upper lapse rate (γ) (see Figure 3.2).

4.3.2 FFT Energy Spectra

Based on the scalar FFT energy plots taken at the top of the ML there is a cascade from the larger to the smaller scales following the $-\frac{5}{3}$ power law (see Figure 3.6). The CBL is fully turbulent at this point but further into the entrainment layer (EL) there are large areas of little or no vertical velocity interspersed with isolated impinging plumes. So the dominant structures are smaller and there is a steeper decay to the lower scales. In this the FFT plots and the contour plots in Figures 3.10 and 3.9 compliment eachother. Furthermore there seems to be adequate scale separation between the dominant turbulent structures and the grid size, as well as isotropic turbulence.

4.3.3 Ensemble and horizontally averaged vertical Potential Temperature $\overline{\theta}$ and Heat Flux profiles $\overline{w'\theta'}$

Schmidt and Schumann point out in [12] that as a convectively mixed layer (ML) grows against a stable lapse rate (γ) overshoot of the plumes to levels above their buoyancy causes a sharp temperature gradient. The sharpest vertical gradient in the area averaged potential temperature ($\overline{\theta}$) profile corresponds to the vertical level at which the average potential temperature (Figure 3.7) differs greatest from that one level above. Once a plume has overshot, envelopment or pinching off (Sullivan et al. [19]) of warm air from above causes a more gradual increase in temperature. Where this occurs is regarded here as the entrainment layer EL. In the averaged potential temperature profile it is represented by an increase in the vertical gradient. On the horizontal plane it would be composed of areas of ML air interspersed with pockets of warmer air from above. The ratio of ML to stable air increases with proximity to the ML. This progression is seen in the average profile as a decrease in the vertical gradient to close to zero (Figure 3.1). Our average potential temperature profiles in Figure 3.7 show a well mixed ML overshooting and growing against γ. CBL growth increases with $\overline{w'\theta'_s}$ and is inhibited by γ. The ML warming rate is strongly influenced by $\overline{w'\theta'_s}$ and γ.

The vertical $\overline{w'\theta'}$ profiles in Figure 3.8 assume the expected shape becoming negative in the EL where the upward moving thermals are relatively cooler than the horizontal average and there is also downward moving warmer air that has been pinched off or folded in. Like Sullivan et al. in [19] and Federovich et al. in [6] we notice the entrainment ratio is less than .2 ($\approx$ .1) for all runs but seems to increase with increased γ inline with Sorbjan's assertion in [13] that moments of $\theta^{'}$ depend on γ. Otherwise, there seems to be self similarity in time and across runs when scaled by $\overline{w'\theta'_s}$ and plotted against scaled height. So the scaled depth of the region of negative $\overline{w'\theta'}$ seems more or less constant whereas Federovich et al. in [6] seem to show a decrease from about .6 to about .2 with increasing Ri and Brooks and Fowler with their slightly different definition in [3] seem to observe slight and contrasting trends with respect to Ri depending on whether the output is time averaged or not.

4.3.4 Visualization of Structures within the Entrainment Layer

Sullivan et al. in [19] show both horizontal and vertical cross sections of their domain within the EL around the inversion (h). Horizontal cross sections of vertical velocity and temperature perturbations clearly show coherent structures with both relatively warm and cool air, associated with up-and-downward velocity. Vertical cross sections show impinging plumes and pockets of trapped warmer air. The weak inversion case seems to show convective overturning with apparent folding of warm stable air. The strong inversion case shows less deformation of the inversion interface and the entrainment event shown in the vertical cross section seems to occur via a narrow downward wisp associated with an impinging plume. In both cases, the downward motion of air from above is closely associated with upward moving impinging plumes.

In our contours of w' and θ' we see the almost spoke like pattern characteristic of the mixed layer (Schmidt and Schumann [12]) at the lower limit of the EL and then distinct plumes become clearer at the inversion and above, where there are coherent areas of warmer and cooler air associated up and downward vertical velocity perturbations (Figures 3.9 and 3.10). This progression is similar to that seen in [7] by Garcia and Mellado. We do see bigger clearer regions of upward moving air in the weak stability case as compared to the the strong stability case. There are pockets of warmer air close to and around the impinging cooler plumes, in line with the concept of wisps being pinched off, or enfolded.

4.4 Local Mixed Layer Heights (h_0^l)

Sullivan et al. [19] used a centred differencing gradient method for determining local CBL height and observed the distributions of $z_i' = z_i - < z_i >$. They observed positive skew in their weak stability cases which they speculated was due to a small number of high reaching plumes. We initially tried a similar method and noticed positive skew, which we found corresponded to local points where the upper variability exceeded the gradient between the ML and the upper atmosphere. So for our purposes the gradient method was rendered unusable

The point of maximum vertical gradient in a tracer profile should correspond to that in a potential temperature profile but the profiles can be quite different. For example a Lidar back-scatter profile which corresponds directly to tracer concentration profile, has a high value in the ML and a low value in the upper atmosphere, similar to step function. Usually the variability within these regions is a lotsmaller than that over the transition region between the two. So the transition region can be identified using a wavelet of dilation corresponding the the depth of the transition zone. This is clearly shown by Brooks in [2] who uses such a wavelet to identify the local EL and then one with narrower dilation to identify the EL limits. The gradient method can also be applied to a Lidar profile but again this can be noisy. Steyn et al. in [15] overcame this by fitting smooth idealized curve to the profile.

In line with this last method, we fit a three lines to the local profile representing the ML, EL and upper layer of constant γ based on the multilinear regression method outlined by Vieth in [22]. This works well with our very simple set up, IE, each local profile consists of a distinct ML and upper region of constant γ. Locally there is not always a clear EL. At points where there is neither a sharp gradient nor a clear EL and some variation in the slope within the ML, a test was needed on the slope of the second line to see if it was significantly less γ. If so, it was considered to be part of the ML.

Brooks and Fowler's three statistically based entrainment zone limits in [3] showed decreasing trend with increase in Ri. Their resulting scaled EL is a lotnarrower than that based on our $\frac{\partial \overline{\theta}}{\partial z}$ profile i.e. .05 - 1.5, and even seems narrower than what would be the 5th and 95th percentile of our local ML heights (see Figure 3.15). Their lowest inversion strength seems to be 1 degree over 100 meters (IE .01 per meter) which is the same as our maximum stability, except of course ours is constant, and their highest is 10 times that. But their lapse rate above is a lot lower ($3k/Km$). So, this difference cannot simply be explained in terms of inversion strength.

We see that the local profiles are very different to the average profile and that local profiles differ from each other (Figures 3.11 and 3.12). The EL is an inherently average phenomena i.e. the range in space or, the range in time, over which the plume heights vary. So it is possible to see a local EL. For example in Figure 3.12 (a) we see a region above the ML which is clearly not part of the stable air above. Here, we can speculate that a plume previously had reached that point and some entrainment of warmer air from above had occurred.

Overall Sullivan et al. [19] show decreased variation in the local heights, with increased Ri as we do. Based on the histograms of our local ML heights in Figure 3.14 we see the range or spread increases with increased $\overline{w'\theta'}_s$ and decreases with increased γ. When scaled by h in Figure 3.15 the spread seems only influenced by γ. So once again there is a cancellation of the effects of $\overline{w'\theta'}_s$ once h is introduced.

4.5 Flux Quadrants

The shape of the average potential temperature profile evolves according to the temperature flux profile. In particular warming in the entrainment layer (EL), and upper mixed layer (ML) is related to the flux of warmer air up or down to that region. Lower in the ML warming is from the thermals or plumes originating at the surface. These plumes become cooler than the horizontal average in the EL where upper stability above the inversion interface causes them to turn downward. Here there are accompanying downward moving pockets of warm air associated with the upward moving plumes. All of this was seen in the visual aids presented by Sullivan et al. in [19].

In [10] Mahrt and Paumier examined the joint distributions of $w^{'}$ and $\theta^{'}$ from measurements taken of mixed layers developed in the flow of cold air masses over a warm current. Their two dimensional representations clearly show the four quadrants: upward warm, upward cool, downward cool and downward warm.

Sorbjan in [13] asserted and demonstrated that the moments involving $\theta^{'}$ particularly in the upper ML and EL are strongly influenced by the upper lapse rate γ. Whereas moments of $w^{'}$ were less so. These effects were seen when the corresponding vertical profiles were scaled by the convective scales (θ^{*} and w^{*}).

Bearing the above three studies in mind we separate the $w^{'}\theta^{'}$ into the four quadrants and plot the average vertical scaled profiles as well as the 2d histograms at h and the EL limits. We can confirm that the upper extrema of the four individual quadrants exceed that of the average and are higher i.e. close to h (Figure 3.16). Higher stability results in a more pronounced peak particularly in the upward cool quadrant profile which corresponds to increased damping and a sharper decrease in velocity. Since warming in this region is associated with downward movement of air from above, the downward warm quadrant is important.

The 2d histograms at each level show increased spread of both $\theta^{'}$ and $w^{'}$ with increased $\overline{w^{'}\theta^{'}}_s$ (Figures 3.18, **??**, 3.19). There is damping of $w^{'}$ with increased γ. To isolate the effects of increased γ we should scale by the convective scales (θ^{*} and w^{*}) .

4.6 h and Δh based on Average Profiles

4.6.1 Reminder of Relevant Definitions

Our heights are defined based on the average vertical temperature gradient the principle length scale being h the vertical location of the maximum. Flux based heights are scaled by h to enable comparison with the frameworks of other studies.

4.6.2 $\frac{w_e}{w^*}$ vs Ri^{-1}

In Figure 3.22 h shows a $\frac{1}{2}$ power law relationship to time indicating we are in the regime outlined by Federovich et al. in [6]. Self similarity of the scaled heat flux profiles vs scaled height in Figure 3.4 indicate a more or less constant entrainment ratio, but also a more or less constant scaled entrainment depth with respect to time. Our Richardson numbers (Ris) increase with respect to time and again grouping according to γ is evident (Figure 3.24).

Kato and Philips successfully related the scaled entrainment rate of penetrative shear driven turbulence in their water-tank experiment in [9] to a dimensionless group formed from the three main characteristics of the flow : the buoyancy jump across the interface, the turbulent velocity of the ML and the depth of the ML. IE

$$\frac{u_e}{u^*} \propto \frac{\rho_0 u^{*2}}{g\delta\rho D} \tag{4.3}$$

Deardorff et al. related their scaled entrainment of penetrative convection to this dimensionless group, substituting the shear driven velocity scale for the convective one, thus forming the now commonly used Richardson number (Ri)for the CBL. Their heights were determined from the vertical heat flux profiles. The heat flux profiles in turn were derived from two successive potential temperature profiles. The resulting relationship between scaled entrainment rate and Ri appears to potentially exhibit both -1 and $\frac{-3}{2}$ power laws.

Sullivan et al.'s data in [19] showed some scatter and they speculated that a power law other than -1 may have described the relationship at Ris smaller than 14. They compare the data to this fit:

$$\frac{w_e}{w^*} = 0.2Ri^{-1} \tag{4.4}$$

Turner in [21] attribute the $-\frac{3}{2}$ power law to mixing that depends on the recoil of impinging eddies. Whereas Federovich et al. in [6] derive it from a best fit approximation of the Ri calculated using the buoyancy jump across the EL to scaled time (after $tN > 100$) and applying the zero order model relationship.

Brooks and Fowler's plot in [3] has relatively little scatter and exhibits a linear relationship (-1 power law) whereas Garcia and Mellado's data in [7] seems asymptotic to a linear relationship.

Our data based on the temperature jump across the entire EL shows a seemingly linear relationship (Figure 3.25).

4.6.3 $\frac{\Delta h}{h}$ vs Ri^{-1}

The EL tops as defined by the point at which the temperature gradient resumes γ seem to be scaled well by h (Figure 3.26). This seems in contrast to the assertion of Garcia and Mellado in [7] about the upper EL i.e. that length and buoyancy in this region are not scaled by the the CBL convective scales. The EL top as defined where the point at which the buoyancy flux decreases to close to zero, when scaled by h is comparable, but has greater scatter (Figure 3.27). But in both cases, the top limit is about $1.15 \times h$, and there is a barely perceptible, possible negative trend.

The scaled lower EL limits based on the increase in potential temperature gradient from zero, show a clearer increase but don't show the same kind of collapse across runs as the upper limit does (Figure 3.26). The scaled lower limit based on the flux profiles however, do collapse well (Figure 3.27). So we could say with some confidence that $\frac{h-z_{f0}}{h} \approx .2$ and this is comparable to Garcia and Mellado's lower EL sublayer.

So the scaled EL as defined by the vertical gradient in the potential temperature profile certainly decreases with respect to time. The scaled EL based on the flux profiles shows slight or no change with respect to time. This is in line to the findings of Brooks and Fowler in [3] even though their definition is slightly different IE $2 \times (z_f - z_{f0})$. But it is in stark contrast to what Federovich et al. show in [6] i.e. $\frac{z_{f1}-z_{f0}}{z_f}$ decreasing from about .6 to about 0.1. This could in part be explained by the difference in vertical resolution since according to Sullivan and Patton in [18] the shape of average heat flux profile in the EL is sensitive to grid size.

Sorbjan in [13] and [14] demonstrates how the surface and lower ML portions of the temperature gradient profile is scaled well by the convective scales but γ becomes more important in the EL. From our potential temperature profiles in Figure 3.7 we see that both γ and $\overline{w'\theta'}_s$ influence the warming of the ML. So this should reflect in particular in the downward flux of warm air from the inversion IE at h. That is, increasing γ seems to result in an increased slightly positive gradient in the upper ML and this should relate to an increase in the downward flux warm air above it, for example at h.

So, first we define the EL lower limit as the point at which the vertical gradient exceeds a positive threshold that's less than γ and the same for all runs, at all times. We try three different values and note that there is a seeming decrease in the scaled magnitude with respect to Ri, bearing in mind the definition of the EL is included in the calculation of $\Delta\theta$ for Ri. Grouping according to γ is evident.

Scaling the vertical potential temperature gradient profiles by γ results in collapse to more or less one curve. The gradient profiles seem to show an increase in the peak gradient as the EL seems to narrow. This trend is apparent with respect to time and across runs. This portion of the profile has been scaled effectively by Sorbjan in [14] using $\frac{\Delta\theta}{\Delta h}$ and Garcia and Mellado using their buoyancy scale $b \approx N^2\delta + [\overline{b_0}(h) - \overline{b}(h)]$ where $\delta \propto \frac{w^*}{N}$ is their length-scale for the upper EL sublayer. Related to $\frac{\Delta\theta}{\Delta h}$ is the entrainment layer stratification parameter $G = \gamma\frac{\Delta h}{\Delta\theta}$ which Federovich et al. found to be constant throughout the quasi-steady state regime IE, $\Delta\theta \propto \Delta h$. This seems to contradict the apparent increase in maximum gradient with decrease in EL depth.

Bibliography

[1] R. Boers. A parametrization of the depth of the entrainment zone. *Journal of Applied Meteorology*, pages 107–111, 1989. → pages

[2] I. M. Brooks. Finding boundary layer height: Appliction of a wavelet covariance transform to lidar backscatter profiles. *Journal of Atmospheric and Ocean Technology*, 20:1194 – 1205, 2003. → pages

[3] I. M. Brooks and A. M. Fowler. An evaluation of boundary-layer depth, inversion and entrainment parameters by large-eddy simulation. *Bundary-Layer Meteorology*, 142:245–263, 2012. → pages

[] T. D. Crum, R. B. Stull, and E. W. Eloranta. Coincident lidar and aircraft observations of entrainment into thermals and mixed layers. *Journal of Climate and Applied Meteorology*, 26:774–788, 1987. → pages

[] J. W. Deardorff. Convective velocity and temperature scales for the unstable planetary boundary layer and for rayleigh convection. *Journal of the Atmospheric Sciences*, 27:1211 – 1213, 1970. → pages

[] J. W. Deardorff. Numerical investigation of neutral and unstable planetary boundary layers. *Journal of the Atmospheric Sciences*, 29: 91 – 115, 1972. → pages

[4] J. W. Deardorff. Prediction of convective mixed-layer entrainment for realistic capping inversion structure. *Journal of the Atmospheric Sciences*, 36:424–436, 1979. → pages

[5] J. W. Deardorff, G. E. Willis, and B. J. Stockton. Laboratory studies of the entrainment zone of a convectively mixed layer. *J. Fluid Mech.*, 100:41–64, 1980. → pages

[] T. H. Ellison and J. S. Turner. Turbulent entrainment in stratified flows. *Journal of Fluid Mechanics*, 6:423–448, 1959. → pages

[6] E. Federovich, R. Conzemus, and D. Mironov. Convective entrainmnent into a shear-free, linearly stratifies atmosphere: Bulk models reevaluated through large eddie simulation. *Journal of the Atmospheric Sciences*, 61:281 – 295, 2004. → pages

[] E. Fedorovich and R. Conzemius. *Large Eddy Simulation of Convective Entrainment in Linearly and Discretely Stratified Fluids*. Kluwer Academic Publishers, 1 edition, 2001. → pages

[7] J. R. Garcia and J. P. Mellado. The two-layer structure of the entrainment zone in the convective boundary layer. *Journal of the Atmospheric Sciences*, 2014. doi:10.1175/JAS-D-130148.1. → pages

[9] H. Kato and O. M. Philips. On the penetration of a turbulent layer into stratified fluid. *J. Fluid Mech.*, 37:644–655, 1969. → pages

[10] L. Mahrt and J. Paumier. Heat transport in the atmospheric boundary layer. *Journal of the Atmospheric Sciences*, 41:3061–3075, 1984. → pages

[11] E. Nelson, R. Stull, and E. Eloranta. A prognostic relationship for entrainment zone thickness. *Journal of Applied Meteorology*, 28: 885–901, 1989. → pages

[12] H. Schmidt and U. Schumann. Coherent structure of the convective boundary layer derived from larg-eddy simulations. *J. Fluid. Mech.*, 200:511–562, 1989. → pages

[13] Z. Sorbjan. Effects caused by varying the strenth of the capping inversion based on a large eddie simulation of the shear free convective boundary layer. *Journal of the Atmospheric Sciences*, 53:2015 – 2023, 1996. → pages

[14] Z. Sorbjan. Similarity of scalar fields in the convective boundary layer. *Journal of the Atmospheric Sciences*, 56:2212 – 2221, 1999. → pages

[15] D. G. Steyn, M. Baldi, and R. M. Hoff. The detection of mixed layer depth and entrainment zone thickness from lidar backscatter profiles. *Journal of Atmospheric and Oceanic Technology*, 16:953–959, 1999. → pages

[16] R. Stull. Inversion rise model based on penetrative convection. *Journal of the Atmospheric Sciences*, 30:1092–1099, 1973. → pages

[17] R. Stull. *An Introduction to Boundary Layer Meteorology*. Kluwer Academic Publishers, 1 edition, 1988. ISBN 9027727686. → pages

[18] P. P. Sullivan and E. G. Patton. The effect of mesh resolution on convective boundary layer statistics and structures generated by large eddie simulation. *Journal of the Atmospheric Sciences*, 58:2395–2415, 2011. doi:10.1175/JAS-D-10-05010.1. → pages

[19] P. P. Sullivan, C.-H. Moeng, B. Stevens, D. H. Lenschow, and S. D. Mayor. Structure of the entrainment zone capping the convective atmospheric boundary layer. *Journal of the Atmospheric Sciences*, 55: 3042–3063, 1998. doi:10.1007/s10546-011-9668-3. → pages

[] H. Tennekes. A model for the dynamics of the inversion above a convective boundary layer. *Journal of the Atmospheric Sciences*, 30: 558–566, 1973. → pages

[20] K. Traumner, C. Kottmeier, U. Corsmeier, and A. Wieser. Convective boundary-layer entrainment: Short review and progress using doppler lidar. *Bundary-Layer Meteorology*, 141:369–391, 2011. doi:10.1007/s10546-011-9657-6. → pages

[21] J. S. Turner. Turbulent entrainment: the development of the entrainment assumption and its application to geophysical flows. *J. Fluid Mech.*, 173:431–471, 1986. → pages

[22] E. Vieth. Fitting piecewise linear regression functions to biological responses. *Journal of Applied Physiology*, 67:390–396, 2011. → pages